Aerodynamic and Flow Structure Analysis of Iced Wind Turbine Airfoil

by

Zahra Maleksabet

A thesis presented to Lakehead University

In fulfilment of the

thesis requirement for the degree of

Master of Applied Science

In

Mechanical and Mechatronics Engineering

Thunder Bay, Ontario, Canada, 2025

I hereby declare that I am the sole author of this thesis.

I authorize Lakehead University to lend this thesis to other institutions or individuals for the purpose of scholarly research.

Zahra maleksabet

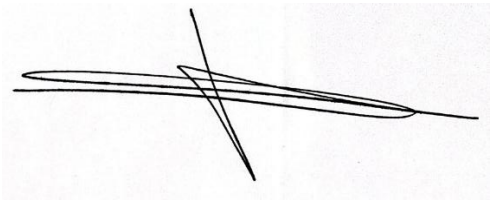

I further authorize Lakehead University to reproduce this thesis by photocopying or by other means, in total or in part, at the request of other institutions or individuals for the purpose of scholarly research.

Zahra maleksabet

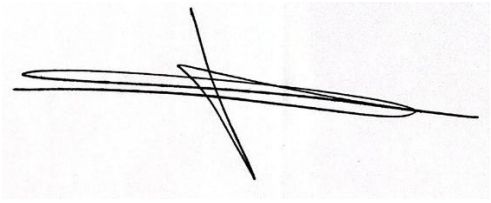

Lakehead University requires the signatures of all persons using or photocopying this thesis. Please sign below and give address and date.

Abstract

The issue of icing on wind turbines presents a significant operational challenge, especially in northern regions of Canada, where cold climates and harsh winter conditions prevail. This buildup of ice increases mechanical stress on the turbines, potentially resulting in costly maintenance and even operational failures. Ice formation alters the aerodynamic properties of the blades, increasing drag, which can severely reduce performance, leading to energy losses. Two primary types of ice profiles that occur in such environments are glaze and rime. In this study, in the first section, the impact of two experimental ice profiles (glaze and rime) on the aerodynamic characteristics of the NACA 64_3-618 airfoil are investigated and compared with the clean airfoil. Large Eddy Simulation is used to do the simulation, at a Reynolds number of 137,000, with angles of attack ranging from -10° to 10° with 5° step. Also, the aerodynamic characteristics of a parametric ice profile on the mentioned airfoil are studied and compared with the clean airfoil, in addition to two experimental ice profiles. The results indicate that the lift coefficient increases consistently with the angle of attack across all iced airfoils. However, the drag coefficient exhibits fluctuating behaviour due to the varying aerodynamic profiles caused by the different ice profiles. Glaze ice significantly increases drag, particularly at higher angles of attack, leading to a more pronounced reduction in aerodynamic efficiency compared to rime ice. Furthermore, in all iced cases, the aerodynamic performance moves forward by 5° compared to Base. The second section investigates the flow structures of glaze and rime and the comparison with the clean airfoil at an angle of attack of 10°. Instantaneous flowfield data at the 30th-second timestep is analyzed through flow visualization techniques, including streamlines, velocity contours and Q-criterion iso-surfaces. Results reveal that ice accretion significantly alters separation points, enhances flow instability, and accelerates the transition to turbulence. The study also examines friction coefficients (C_f) to pinpoint separation and reattachment locations. Furthermore, turbulent kinetic energy and Reynolds stress components are evaluated, showing increased turbulence intensity and energy dissipation due to icing.

Keywords: wind turbine airfoil, atmospheric icing, aerodynamic characteristics, coherent structures

Acknowledgements

First and foremost, I would like to express my deepest gratitude to my supervisor, Dr. Ali Tarokh, for his exceptional guidance, support, and encouragement throughout my graduate studies. His patience and insightful advice have been crucial in shaping both my research and my personal growth as a researcher. I am truly grateful for his mentorship and for the countless ways he has helped me navigate this journey. I would also like to sincerely thank my co-supervisor, Dr. Janusz Kozinski, for his invaluable support and feedback. His expertise and encouragement have been a crucial part of my academic development, and I deeply appreciate the time and effort he has dedicated to my work.

Additionally, I would like to extend my appreciation to my committee members, Dr. Kefu Liu and Dr. Ahmed Elshaer, for their valuable insights and constructive feedback. Their expertise has greatly contributed to strengthening my work, and I am grateful for their time and commitment.

Beyond academia, I owe everything to my family back home in Iran. Their unwavering love, sacrifices, and endless support have been my greatest source of strength. Despite the distance, their belief in me has given me the motivation to persevere through challenges and strive for success. This achievement is as much theirs as it is mine, and I dedicate this work to their unconditional support.

To my family, whose support and sacrifices have made this journey possible…

Table of Contents

List of Figures

List of Tables

1. Introduction

1.1. Literature Review

The global demand for wind energy is rising, largely due to climate change concerns linked to fossil fuel use. In Canada, wind energy capacity installations have surged in recent years, averaging 1,012 MW per year. Notably, over 80% of this capacity is concentrated in three provinces: Ontario (5,436 MW, 40%), Quebec (3,882 MW, 29%), and Alberta (1,685 MW, 13%). This trend is anticipated to improve, with a projected increase of 510 MW annually until 2040 [1]. However, wind turbines in the cold climate of Canada and the humid climate are encountering challenges related to atmospheric icing. Ice formation on turbine blades can significantly diminish efficiency, reduce the operational lifespan of wind turbines, increase noise and vibrations, and pose safety hazards because of the danger of ice shedding. Studies indicate that icing can lead to an annual energy production (AEP) loss of up to 17% and a depletion in efficiency by 20-25% [2–6]. Icing happens when subcooled water droplets strike the cold surfaces of turbine blades. Various factors influence this process, including temperature, droplet size, liquid water content and surface area. Two main types of ice accretion are observed under different climates: glaze and rime. Rime emerges when droplets freeze upon immediate contact with a cold surface, typically growing into the airstream. In contrast, glaze develops when droplets flow downstream before freezing, often resulting in irregular shapes resembling horns [4,6]. While numerous experimental studies have extensively examined the impact of ice formation on the aerodynamic coefficients of wind turbine blades [7–13], the high costs and specialized equipment required for such tests have led to an increasing reliance on simulations. These simulations, leveraging both commercial and open-source tools, allow for a detailed analysis of the complex phenomena involved in ice accretion.

Martini et al. [14] conducted a comprehensive review highlighting essential components in icing simulations, such as aerothermodynamics, multiphase flows, and heat and mass transfer. Their findings underline that factors like airfoil type and angle of attack are crucial in ice formation, which then impacts turbine blade aerodynamics, underscoring the importance of these variables in accurately modelling and mitigating icing effects. Various studies have approached the problem from different perspectives, each contributing insights into how ice

impacts energy production and aerodynamic efficiency. For instance, Homola M. et al. [14] in 2010 investigated the performance of the NACA 64-618 airfoil under different atmospheric conditions. Their use of the k-ε turbulence model revealed that ice, particularly glaze, consistently reduced lift coefficients. Similarly, Virk M. et al. [6] also focused on the NACA 64-618 airfoil but examined the effects of the angle of attack on ice buildup near the blade tip. Their findings showed that smaller angles of attack led to reduced ice mass and thickness near the tip of a blade, a critical insight for understanding how turbines can be designed to mitigate ice formation. As research progressed, more sophisticated models and methods were developed to further unravel these complex interactions. In 2014, Etemaddar M. et al. [5] assessed the impact of several system and atmospheric parameters on ice profiles. Their findings extended beyond aerodynamic effects, revealing how ice can alter both power and thrust performance at different wind speeds.

Szilder K. and Yuan W. [15] Followed by their work in 2015, which also used numerical simulations to evaluate the effect of ice on the SD7037 airfoil. They found that colder conditions, regardless of droplet size, resulted in reduced ice mass but increased aerodynamic penalties, particularly with glaze. In a step towards improving simulation fidelity, Villalpando F. et al. [16] in 2016 modelled the wall of the NACA 63-415 airfoil as a permeable boundary to predict the ice appearance on the airfoil, finding good agreement between their simulations and experimental data. Meanwhile, Pedersen M. and Sørensen H. [17] proposed a unified CFD model that proved effective in predicting wind turbine power reduction because of ice accretion. Yirtici O. et al. [4], who used the Blade Element Momentum (BEM) method alongside an ice prediction appliance, reinforced these findings to explore the energy reductions incurred by iced blades, particularly the NACA 64-618 and S809 airfoils. More recent studies have built on these findings with advanced computational approaches.

Gantasala S. et al. [2] in 2019 automated the ice shape creation process for the NREL 5 MW wind turbine, showing how symmetrical icing reduced loads while asymmetrical icing increased them, leading to increased vibration risks. Wang Q. et al. [18] introduced the Improved Multi-Shot Icing Computational Model (IMSICM) to better simulate ice accretion under yaw conditions, showing how ice can form differently depending on wind direction. Li S. and Paoli R. [19] further

explored this topic using OpenFOAM to simulate ice accretion on the NACA 0012 airfoil and ONERA M6 wing, noting how the ice shape significantly alters pressure distribution, especially near the blade tip. The impact of atmospheric conditions on turbine performance has been a central focus in recent years. For instance, Sahin M. and Farsadi T. [20] examined the NREL 5 MW wind turbine and found that even light ice accumulation can significantly affect turbine parameters like rotor power, pitch angle of the blade and speed, especially in below-rated wind speed regions. Similarly, Bodenlle-Toral D. et al. [21] examined the effect of snow and ice on the NREL PHASE VI wind turbine to simulate radial ice accretion and its subsequent impact on lift and drag coefficients, finding a 33% rise in drag and a 9% diminution in lift. Also, turbulence models and ice-roughness interactions have been refined [25].

Montoya L. et al. [22] investigated how surface roughness models (e.g., Shin et al. and beading models) and turbulence models like Spalart-Allmaras affect icing outcomes. They noted that roughness plays a critical role in determining aerodynamic losses, particularly in glaze conditions where drag increased by 70%. Bornhoft B. et al. [23] in 2024 pushed the boundaries of simulation techniques, using wall-modelled large eddy simulation (WMLES) to capture the influences of various ice geometries on a NACA 23012 airfoil. Their detailed modelling revealed that while WMLES performed well for glaze, capturing critical lift and drag changes, rime ice needed extra grid refinement to accurately simulate the aerodynamic forces. Similarly, Rotich I. and Hilda Chepkirui H. [24] expanded the scope of icing research by examining the combined effects of liquid water content, ambient temperature and median volume diameter on ice accretion dynamics, finding that larger droplet sizes and colder conditions lead to greater ice mass and reduced aerodynamic efficiency.

1.2. Present study

Previous research has primarily focused on simulating ice accretion on wind turbine blades with the use of various CFD models, with many studies employing Reynolds-Averaged Navier-Stokes (RANS) simulations. Nonetheless, RANS models rely on assumptions and averaging variables such as velocity and pressure, which can introduce inaccuracies, particularly in capturing turbulent flow transitions. To enhance the accuracy of flow structure analysis and

aerodynamic characteristics assessment of an iced airfoil, this study utilizes Large Eddy Simulation (LES) as a more advanced and precise approach. The investigation includes two experimentally obtained ice profiles (glaze and rime) along with a parametric ice profile. The aerodynamic characteristic of the parametric iced airfoil is compared not only to a clean airfoil but also among the different experimental ice profiles to identify similarities and variations in their aerodynamic behaviour.

Turbulence is a fundamental yet complex phenomenon in fluid mechanics, influencing a wide range of engineering and scientific applications, from aerodynamics to environmental studies. Understanding turbulence and its intricate structures has been the subject of extensive research for over a century. Early studies by Horning [25] and Hunt et al. [26] laid the foundation for describing turbulent flow characteristics, including eddies, stream structures, and convergence zones. These pioneering works provided essential insights into the chaotic nature of turbulence, which later guided the development of computational modeling techniques. Over time, advancements in turbulence research have led to the formulation of various modeling approaches, allowing engineers and scientists to predict turbulent behavior with increasing accuracy. Among the various turbulence modeling techniques, Reynolds-Averaged Navier-Stokes (RANS) and Large Eddy Simulation (LES) have emerged as two dominant approaches. Wilcox [27] made significant contributions to turbulence modeling by refining the RANS framework, which remains widely used in industrial applications due to its computational efficiency. However, RANS models rely on time-averaged equations, which can oversimplify complex turbulent structures, especially in highly unsteady flows. In contrast, LES provides a more detailed representation by directly resolving large-scale turbulent structures while modeling the effects of smaller eddies using subgrid-scale models. The comparative study by Rodi [28] demonstrated the strengths and limitations of LES and RANS in predicting turbulent flow around bluff bodies, highlighting the superiority of LES in capturing unsteady and three-dimensional flow features.

The increasing adoption of LES in computational fluid dynamics (CFD) simulations has been driven by its ability to provide more accurate representations of turbulent flow structures. Zhiyin [29] provided a comprehensive review of the past, present, and future of LES, emphasizing its growing role in fluid dynamics research. Sarlak [30] further explored the effects of Reynolds

number and subgrid-scale modeling in LES of an SD7003 airfoil, demonstrating the sensitivity of LES predictions to these parameters. Recent validation efforts, such as those conducted by Shaukat et al. [31], have strengthened the credibility of LES by introducing new metrics to assess its accuracy in urban wind studies. Furthermore, Davidson [32] compiled extensive knowledge on turbulence modeling, offering a theoretical framework that supports both RANS and LES methodologies.

The study of turbulence is not limited to computational modeling but also extends to understanding physical flow phenomena, such as laminar separation bubbles and their interaction with free-stream turbulence. Jaroslawski et al. [33] investigated the disturbance growth in a laminar separation bubble, revealing how free-stream turbulence can influence boundary layer transition and flow separation. These findings are crucial for aerodynamic applications, where accurate predictions of flow separation and reattachment play a significant role in optimizing airfoil and vehicle designs. Despite the progress in turbulence modeling, challenges remain in accurately predicting high-Reynolds-number flows, resolving near-wall turbulence, and improving computational efficiency. As computational power continues to grow, LES is expected to become more accessible for a broader range of applications. Ongoing research efforts aim to refine subgrid-scale models and hybrid approaches that combine LES and RANS to leverage the strengths of both methods. By continually improving turbulence modeling techniques, researchers can enhance the predictive capabilities of CFD, leading to better performance optimization in aerospace, energy, and environmental engineering.

In addition to the objectives that were mentioned earlier, the second part of the study aims to analyze the impact of ice accretion on the flow structures around a wind turbine airfoil, focusing on coherent structures and turbulence kinetic energy (TKE). Ice formation significantly alters the aerodynamic performance of airfoils, influencing vortex dynamics, flow separation, and turbulence characteristics. By using large eddy simulation (LES), this research investigates how ice-induced surface roughness modifies the flow structures compared to a clean airfoil. The primary objective of this study is to investigate how ice accumulation affects coherent structures and TKE distribution over the wind turbine airfoil. By comparing an iced airfoil to a clean one, the study aims to characterize changes in vortex dynamics, flow separation, and turbulence intensity.

The results will contribute to a deeper understanding of aerodynamic degradation due to ice accretion, offering insights that could inform future design improvements and mitigation strategies for wind turbine performance in cold climates.

2. Methodology

2.1. Governing Equations

The first step for governing equations is mass and momentum conservation equations known as Navier-Stokes which are provided as follows:

$$\frac{\partial U_i}{\partial x_i} = 0 \tag{1}$$

$$\frac{\partial U_j}{\partial t} + U_i \frac{\partial U_j}{\partial x_i} = -\frac{1}{\rho}\frac{\partial p}{\partial x_j} + \vartheta \frac{\partial^2 U_j}{\partial x_i^2} \tag{2}$$

where U, x, ρ, p and ϑ represent velocity, distance, density, pressure and kinematic viscosity [34] and i, j and k represent the indicators in x, y and z directions. The goal of Large Eddy Simulation (LES) is to solve the large-scale turbulence structure and model the subgrid range structures according to the filter applied to each variable in equations which must be homogeneous [35]. Consequently, the flow field is separated and solved into two parts, the first part is the resolved turbulence structures, and the second one is the filtered and modelled turbulence structures [36]. Involving the filter to every one of the variables, the equations that are filtered are attained,

$$\frac{\partial \overline{U}_j}{\partial t} + U_i \frac{\partial \overline{U}_j}{\partial x_i} = -\frac{1}{\rho}\frac{\partial \bar{p}}{\partial x_j} + \vartheta \frac{\partial^2 \overline{U}_j}{\partial x_i x_i} - \frac{\partial \tau_{ij}}{\partial x_i} \tag{3}$$

where τ and t represent the stress tensor and time respectively [34] and τ is calculated as follows:

$$\tau_{ij} = \overline{U_\iota U_J} - \overline{U}_\iota \overline{U}_J \tag{4}$$

To solve this problem, one more model needs to close the system of equations and contemplate the effect of subgrid scale stresses, τ_{ij}. The equation can be obtained from an additional model, which is called local dynamic k-equation proposed by Kim and Menon. [37,38]. This one-equation model is used to replicate subgrid scale (SGS) turbulent kinetic energy (TKE) [34]. The definition of the SFS turbulent kinetic energy is:

$$k_{SGS} = \frac{1}{2}(\overline{u_k u_k} - \bar{u}_k \bar{u}_k) \tag{5}$$

where k represents the turbulent kinetic energy [34] and the transport equation is:

$$\frac{\partial k_{SFS}}{\partial t} + \bar{u}_i \frac{\partial k_{SFS}}{\partial x_i} = -\tau_{ij}\frac{\partial \bar{u}_i}{\partial x_j} + \varepsilon_{SFS} - \frac{\partial}{\partial x_i}(\vartheta_{SFS}\frac{\partial k_{SFS}}{\partial x_i}) \tag{6}$$

ε_{SGS} is the SGS dissipation rate [34] which is modelled using:

$$\varepsilon_{SGS} = C_{\varepsilon} \frac{k_{SGS}^{\frac{3}{2}}}{\bar{\Delta}} \tag{7}$$

Also, subgrid scale stress tensor [34] is:

$$\tau_{ij} = -2C_{\tau}\bar{\Delta}k_{SGS}^{\frac{1}{2}}\bar{S}_{ij} + \frac{2}{3}\delta_{ij}k_{SGS} \tag{8}$$

C_{ε} and C_{τ} are considered by using dynamic procedures. The test filter is usually considered to be twice the grid filter. [34,37]. Δ and S represent the cell volume and strain rate tensor respectively [34]. The resolved TKE at the test filter scale is:

$$k_{test} = \frac{1}{2}(\widehat{\overline{u_k}\overline{u_k}} - \widehat{\overline{u_k}}\,\widehat{\overline{u_k}}) \tag{9}$$

C_{τ} for this model is defined as [34]:

$$C_{\tau} = \frac{L_{ij}\sigma_{ij}}{\sigma_{lm}\sigma_{lm}} \tag{10}$$

which

$$\sigma_{ij} = -\Delta k_{test}^{\frac{1}{2}}\widehat{\overline{S_{\iota J}}} \tag{11}$$

And

$$C_{\varepsilon} = \frac{\hat{\Delta}}{k_{test}^{\frac{3}{2}}}((\vartheta + \vartheta_{SGS})(\frac{\partial\widehat{\overline{u}_{\iota}}}{\partial x_J}\frac{\partial\overline{u}_{\iota}}{\partial x_J}\,\frac{\partial\widehat{\overline{u}_{\iota}}}{\partial x_j}\frac{\partial\widehat{\overline{u}_{\iota}}}{\partial x_j})) \tag{12}$$

Consequently, the model has no free parameters, with all coefficients being established from the smallest resolved scales [34].

2.2. Numerical Method

LES enables a detailed capture of flow structures and provides deeper insights into the aerodynamic parameters such as velocity and pressure distributions. To run the simulations, finite-volume code with the usage of software OpenFOAM v9 [39] is used. Velocity and pressure fields are solved using an algorithm named PIMPLE which stands for PISO (pressure implicit with splitting of operation) in SIMPLE (Semi-Implicit Method for Pressure-Linked Equations). Table 1 shows the details of the discretization method that is used in this study.

Table 1: Discretization methods used in the present study

Term	**Discretization Method**	**Discretization Method**
ddtSchemes	backward	Gauss linear
gradSchemes (default)	Gauss linear	Gauss linear
grad(k)	cellLimited Gauss linear 0.5	Gauss linear corrected
div(phi,U)	Gauss LUST grad(U)	linear
div(phi,k)	Gauss limitedLinear 0.5	corrected

2.3. Geometry and Mesh Topology

This study focuses on the NACA 64_3-816 airfoil, commonly utilized in the tip section of wind turbine blades where ice is mostly tended to form. Modelling ice profiles typically involves solving heat and mass transfer equations alongside the Navier-Stokes equations, which is computationally intensive [18]. To streamline the process, predefined ice profiles, are employed. In this research, as it is presented in Figure 1, including the clean airfoil which is called Base in this study in Figure 1(a), three distinct ice profiles are analyzed to study their effects on aerodynamic characteristics. Glaze and rime are the experimental ice profiles that have been chosen as Ice-1 and Ice-2, respectively (Figure 1(b) and 1(c)) [5]. Furthermore, a parametric ice profile is developed by combining iced airfoils of NACA 0012 and NACA 63-415 to propose an ice profile specific to NACA 64_3-816 airfoil [2] which is shown as Ice-3 in Figure 1(d).

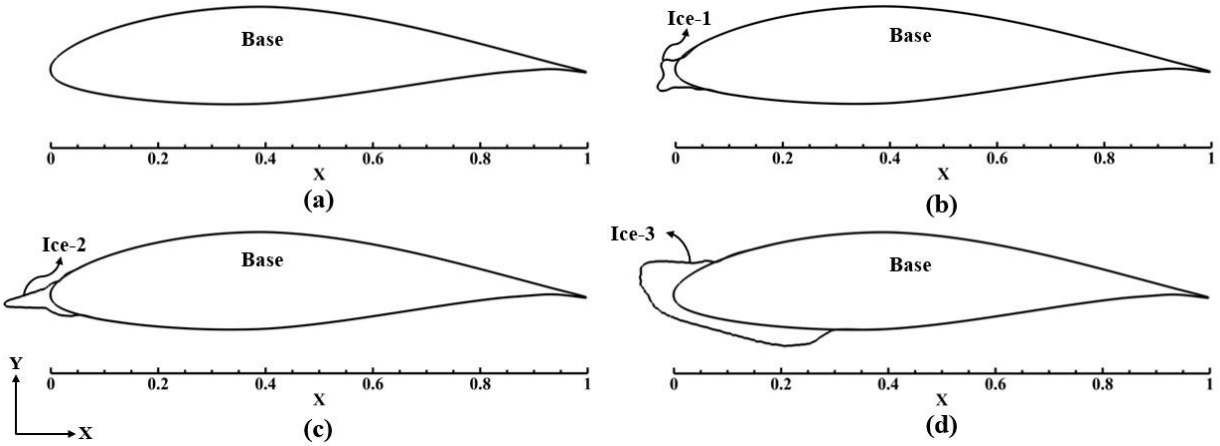

Figure 1: (a): Base, (b): Ice-1 (experimental ice profile for glaze) [5], (c): Ice-2 (experimental ice profile for rime) [5], (d): Ice-3 (parametric ice profile) [2]

The simulations are conducted at the Reynolds number of 137,000 based on chord length, in several angles of attack ranging from -10° to 10° by 5° step. For the mentioned Reynolds number there are experimental results for a diverse range of angles of attack with the same airfoil [40,41] that are accordingly used to validate the simulation. The computational domain extends 10 chord lengths downstream, 4 chord lengths upstream, and 4 chord lengths above and below the airfoil [42,43]. A spanwise extension of 0.2 chord lengths is included to resolve three-dimensional boundary layers and capture large eddies accurately [34,41,44]. The unstructured mesh is generated using one of OpenFOAM utilities, snappyHexMesh and mesh topology for four cases of Base, Ice-1 an Ice-2 are presents in Figure 2, Figure 3, Figure 4 and Figure 5.

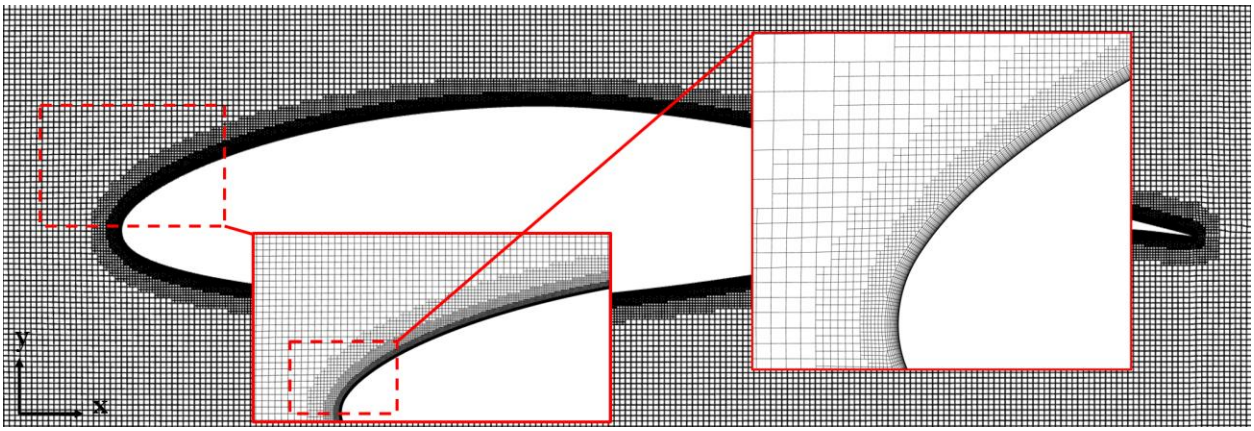

Figure 2: Mesh topology and boundary layer for Base

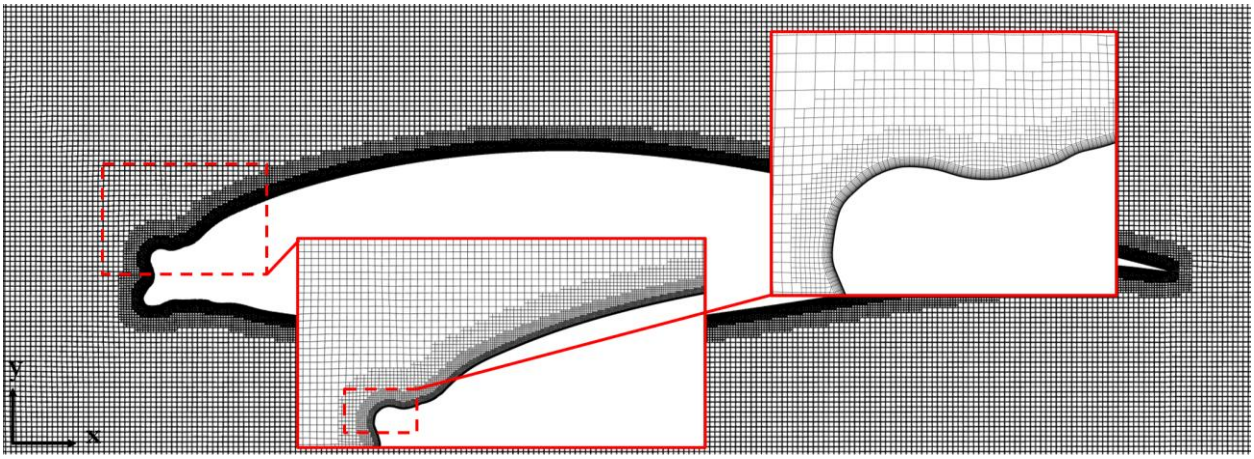

Figure 3: Mesh topology and boundary layer for Ice-1

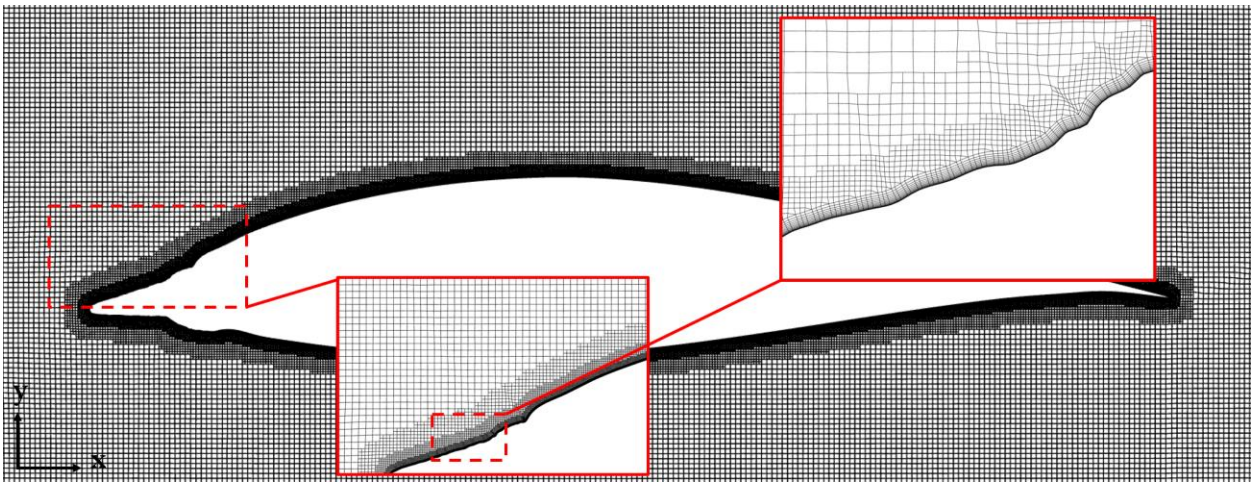

Figure 4: Mesh topology and boundary layer for Ice-2

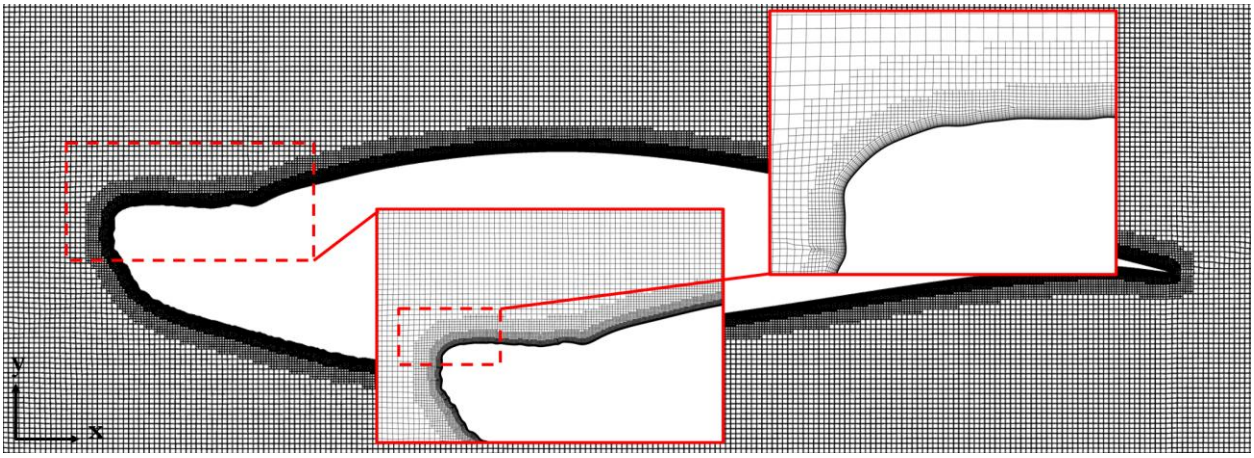

Figure 5: Mesh topology and boundary layer for Ice-3

Table 2 shows the details of the mesh for Base, Ice-1, Ice-2 and Ice-3. The first layer of thickness, number of boundary layer and expansion ration are set in snappyHexMesh file while the rest of the details in Table 2 can be checked by checkMesh.

Table 2: Mesh parameters for Base, Ice-1, Ice-2 and Ice-3.

Case	y^+	**First layer thickness (mm)**	**Number of boundary layer**	**Expansion ratio**	**Number of grids**
Base	0.65	0.005	15	1.15	7,607,568
Ice-1	0.41	0.003	15	1.15	7,818,384
Ice-2	0.47	0.003	14	1.2	7,779,280
Ice-3	0.51	0.003	15	1.2	7,971,600

For the grid independency, three different mesh resolutions are examined for Base and the number of mesh starts from 1.7 million for grid 1 to 7.6 million for grid 3. Table 3 shows the details of the grid independency and the error both lift and drag coefficient has with the experimental results [40,41].

Table 3: Grid independency

case	**Number of mesh**	C_l	C_d	**Error (C_l)**	**Error (C_d)**
grid 1	1,746,264	0.07	0.055	68.2%	27.9%
grid 2	3,588,704	0.26	0.05	18.2%	16.3%
grid 3	7,607,568	0.254	0.048	15.4%	11.6%

The velocity profile for three different grids for the near-wall region is presented in Figure 6 which shows the efficiency of domain and mesh topology. As a result, grid 3 has been chosen as Base number of meshes with a 15.4% error in lift and 11.6% error in drag coefficients compared to experimental results [40,41].

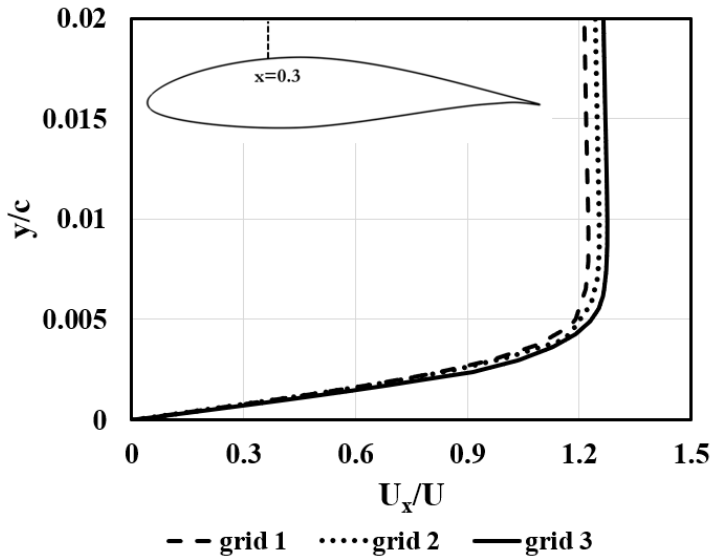

Figure 6: Comparison of three different velocity profiles for grid 1, grid 2 and grid 3 at x/c=0.3

2.4. Boundary and Initial Conditions and Validation

For boundary conditions, velocity has a fixed value of 2.055 m/s at the inlet to satisfy the Reynolds number and zeroGradient at the outlet. Also, a fixed value of zero is set on the airfoil for velocity. For the lower and upper walls of the domain, the boundary condition is considered as slip. The pressure boundary condition at the inlet is set as zeroGradient and a fixed value of zero at the outlet and for the airfoil, the lower and upper wall of the domain is set as zeroGradient. Turbulent kinetic energy is set to 10^{-8} for the inlet and airfoil, while for the rest of the boundaries, it is set to zeroGradient. More details for boundary conditions are presented in Figure 7.

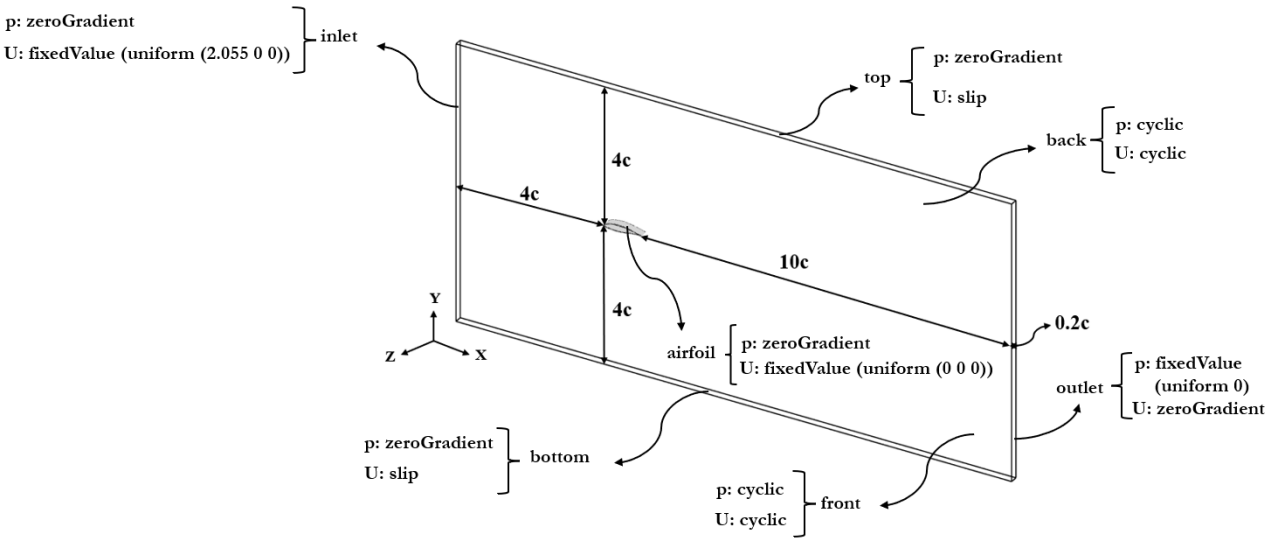

Figure 7: Domain and boundary conditions

To decrease the computational cost and simulation time, the flow field is initialized using k-ω SST steady-state. For LES, the simulation is done in 4 FTT (flow through time) equal to 60 c/U. In the first 2 FTT, the flow has the chance to stabilize and in the next 2 FTT the average is considered for the flow field parameters. Courant Friedrichs Lewy, which is called CFL, is fixed to 0.8 and time steps change during the simulation to satisfy the CFL. For validation of the simulation, the lift coefficient in different angles of attack is compared to experimental results in the mentioned Reynolds number [40,41] as shown in Figure 8. As presented in Figure 8, as the lift coefficient is in acceptable agreement with the results from experiments, it has a minimum error of 8.5% with the experimental results in an angle of attack equal to 5.

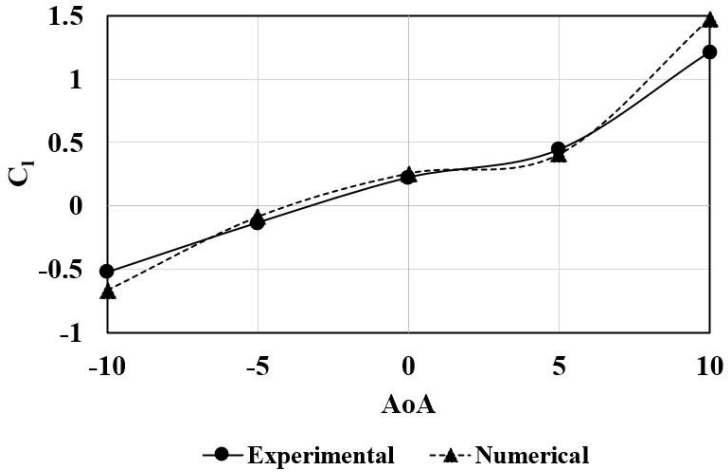

Figure 8: Validation for lift coefficient [40,41]

Also, Figure 9 shows the drag coefficient comparison between the current study and the experimental results. As is presented below, the experimental trend for drag coefficient is followed by the simulation results and there is a good agreement between the experimental and numerical results.

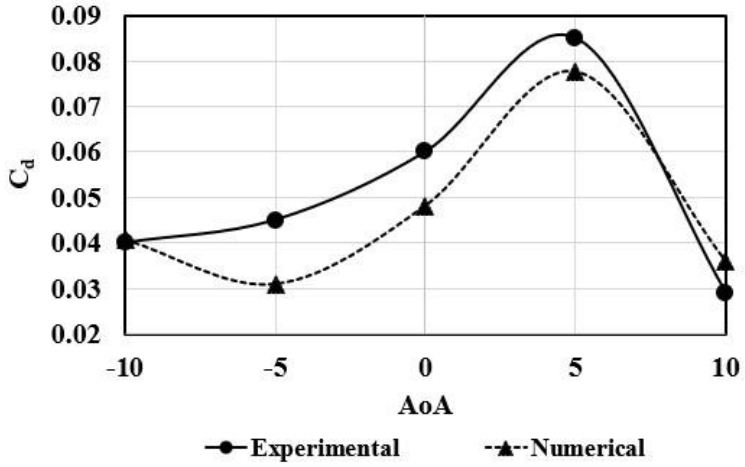

Figure 9: Validation for drag coefficient [40,41]

3. Results and Discussion: Aerodynamic Analysis

3.1. Overview

In this section the aerodynamic characteristics such as lift, drag, and aerodynamic performance for four models: Base, Ice-1, Ice-2, and Ice-3 over a range of angles of attack (AoA) (-10° to 10° with 5° step) are analyzed. The first section focuses on evaluating the impact of two experimental ice profile cases (Ice-1 and Ice-2) on the aerodynamic features of the airfoil and the comparison to Base. In the second section the parametric ice profile case (Ice-3) is examined, comparing it not only to Base but also to Ice-1 and Ice-2. This approach provides a deeper understanding of the similarities and differences between parametric and experimental cases of ice profiles.

3.1.1. Aerodynamic characteristics of Ice-1 and Ice-2

Figure 10(a), 5(b), and 5(c) present the drag coefficient, lift coefficient, and aerodynamic performance for Base, Ice-1, and Ice-2, respectively. In Base case, the drag coefficient gradually rises with an increase in AoA, attaining its peak at 5° before declining at higher angles. Meanwhile, the lift coefficient steadily rises with the increase in AoA, resulting in an aerodynamic performance trend that closely follows the upward trajectory of the lift coefficient. For Ice-1, the drag coefficient decreases as the angle of attack rises, reaching its lowest value at 0°, before increasing at positive angles. Since the lift coefficient follows a continuous upward trend, the aerodynamic performance also increases from negative angles of attack, peaking at approximately 5°. In Ice-2, the drag coefficient demonstrates a fluctuating behaviour, whereas there is an increase in the lift coefficient consistently concerning AoAs. The aerodynamic performance reaches its highest value at an angle of attack of 5°.

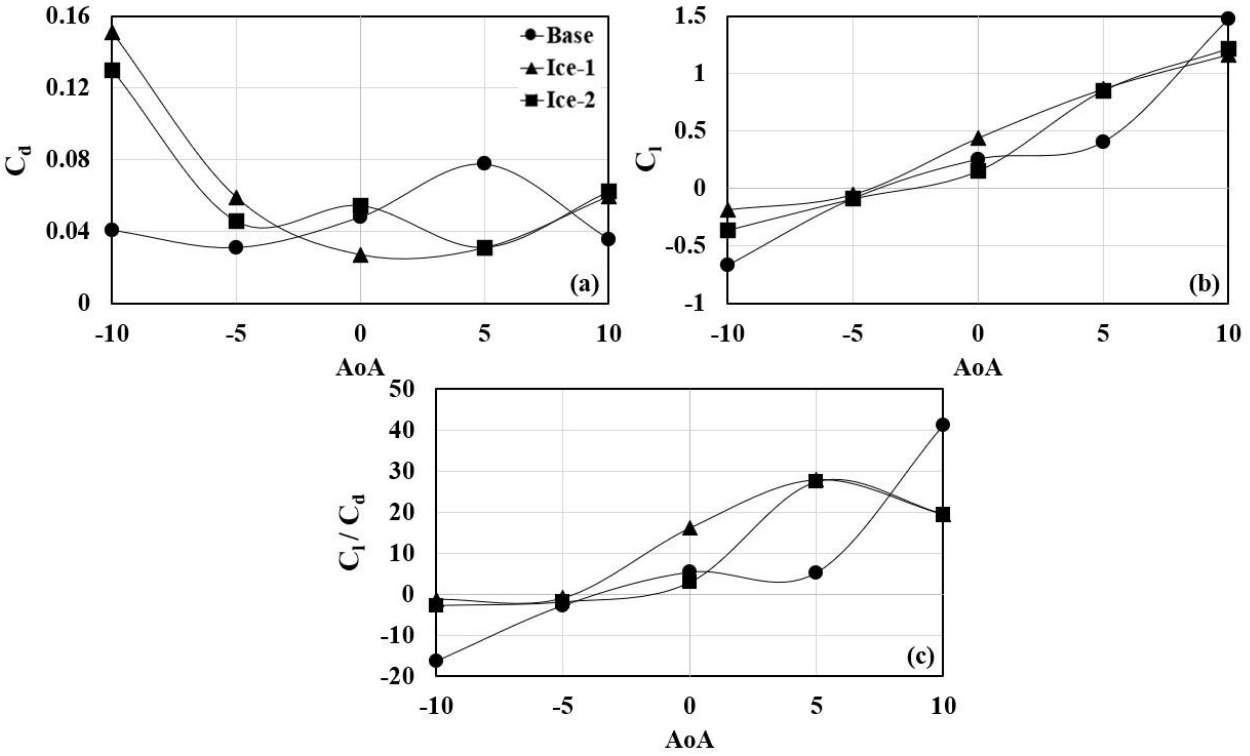

Figure 10: (a) Drag coefficient for Ice-1, Ice-2 and Base, (b) lift coefficient for Ice-1, Ice-2 and Base, (c) aerodynamic performance for Ice-1, Ice-2 and Base

The variations in drag coefficient behaviour for Base case are analyzed using the velocity contours in Figure 11 in divergent angles of attack. At approximately -10° (Figure 11 (a)), flow separation occurs on the lower area around x/c = 0.6 because of the adverse pressure gradient (APG) that forms a thin separation layer that extends toward the trailing edge (TE). This separation contributes to pressure drag, increasing the drag coefficient. As the AoA rises, the adverse pressure gradient weakens on the lower surface concurrently becoming more pronounced on the upper surface. At positive AoAs, the flow remains attached to the lower surface, whereas the separation region on the upper surface thickens, initiating around x/c = 0.5. By AoA = 5° (Figure 11(d)), the largest separation region develops on the upper surface, leading to the peak drag coefficient. At higher AoAs, a locally high-velocity region on the upper surface helps maintain attached flow, preventing separation and reducing the drag coefficient. In Base case, the lift coefficient is primarily influenced by the distribution of pressure, which is visualized using the pressure coefficient in Figure 12. At negative angles of attack (Figure 12(a) and 7(b)), a large low-pressure zone forms on the lower area, generating a negative lift coefficient.

Additionally, the pressure coefficient jumps at negative angles indicate flow separation points over the airfoil. As the AoA increases, the low-pressure region diminishes on the lower area and shifts to the upper area, leading to a positive lift coefficient. In AoA = 10° (Figure 12(e)), a significant pressure deviation between the lower and upper surfaces is observed along the entire airfoil, producing the highest positive lift coefficient. The aerodynamic performance, defined as the ratio of C_l to C_d , follows a similar trend to the lift coefficient, increasing with the increase in AoA and reaching its peak at AoA = 10°.

As shown in Figure 10(a), the drag coefficient for Ice-1 is 272% higher than Base in AoA=-10°. The reason for that is the separation region on the lower side of the airfoil that happens because of the presence of the ice, which induces flow separation from the leading edge (LE) to the TE (Figure 11(a)). As the AoA increases, the separation region on the lower area transforms into a separation bubble limited to the LE which energizes the boundary layer, keeping the flow attached to the surface [23], results in a significant reduction in the drag coefficient (Figure 11(b) and 6(c)). In 0° angle of attack, Ice-1 exhibits its minimum drag coefficient, which is 43% lower than Base case. As the angle of attack continues to increase, the separation region happens on the upper surface around x/c = 0.7 due to the adverse pressure gradient, slightly increasing the drag coefficient. For Ice-1 at high negative angles of attack (AoA=-10°), the negative lift coefficient is lower than Base case, because of the reduction in negative distribution of pressure on the lower side of the airfoil that can be seen in Figure 12(a) and 7(b).

As the AoA increases, the low-pressure region shifts to the upper area, producing a positive lift. Additionally, the separation bubble prevents early separation, enhancing the lift coefficient. At AoA = 5°, the lift coefficient for Ice-1 is 113% higher than that of Base case as presented in Figure 12(d) that there is a big pressure coefficient difference between the two surfaces of Ice-1 compared to Base. However, although the lift coefficient continues to increase with the angle of attack, the rate of increase for Ice-1 is lower than for Base case, leading to a 21% reduction in lift at AoA = 10° compared to Base. This reduction occurs because the flow in Ice-1 detaches around x/c = 0.7, whereas no separation occurs in Base case. Examining aerodynamic performance for Ice-1 reveals an increasing trend from negative angles of attack up

to AoA = 5°, aligning with the reduction in drag. At AoA = 5°, Ice-1 achieves its peak aerodynamic performance, which is 435% higher than that of Base case.

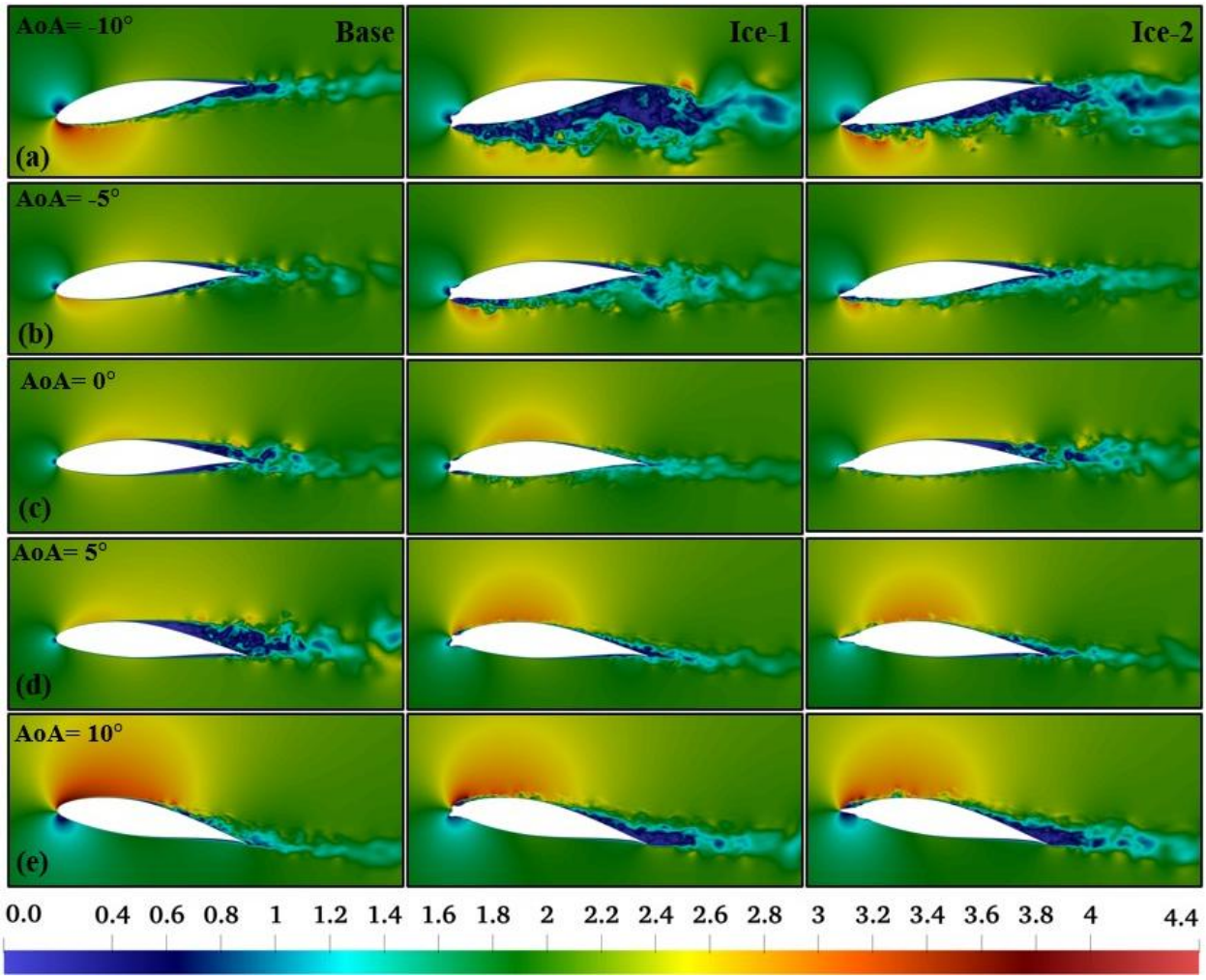

Figure 11: Velocity magnitude contour in (a) AoA= -10°, (b) AoA= -5°, (c) AoA= 0°, (d) AoA=5°, (e) AoA=10° for Base, Ice-1, Ice-2 models.

The drag coefficient exhibits a fluctuating trend for Ice-2, as shown in Figure 10(a), which can be explained by velocity contours in Figure 11. In negative angles of attack, because of the presence of ice on the leading edge, the separation happens on the lower surface of the airfoil which results in a high drag coefficient that is 220% more compared to Base as shown in Figure 11(a) (AoA=-10°). By increasing the angle of attack, the separation point postpones to the trailing edge of the airfoil and the separation region gets thinner, lowering the drag coefficient significantly. As the AoA starts the positive amount, the separation point starts to occur from the middle chord length on the upper area of the airfoil slightly increasing the drag coefficient. In

positive angles of attack, the flow stays attached to the upper surface due to the locally high-velocity region on the upper side which pushes the flow toward the airfoil (Figure 11(d) and (e)). In AoA=5°, the minimum amount for drag happens which is 60% less compared to Base. The lift coefficient can be analyzed through the pressure distribution. As shown in Figure 10(b), the lift coefficient for Ice-2 increases with the AoA. At negative angles of attack, the pressure difference between the lower and upper areas of the airfoil is minimal. At AoA = -10°, a separation region forms on the lower area, leading to a nearly constant pressure region (Figure 12(a)).

As the AoA increases into positive values, a low-pressure region begins to develop on the upper surface, generating a positive lift coefficient that continues to rise with the angle of attack. In AoA = 10°, the distribution of pressure on the lower area of Ice-2 is almost identical to that of Base case (Figure 7(e)) because of the absence of flow separation. However, on the upper area, a low-pressure region forms but gradually weakens toward the trailing edge. Additionally, a noticeable pressure jump at the leading edge in AoA = 10° (Figure 7(e)) indicates the reattachment point after a separation bubble in Ice-2. This separation bubble reduces the lift coefficient. The aerodynamic performance of Ice-2 remains relatively constant at negative AoAs. However, as the angle of attack shifts into positive values, performance improves, reaching its peak at AoA = 5°, where it is 424% higher than Base case due to the significantly greater lift coefficient at this point. Beyond 5°, aerodynamic performance declines as the drag coefficient increases with the angle of attack.

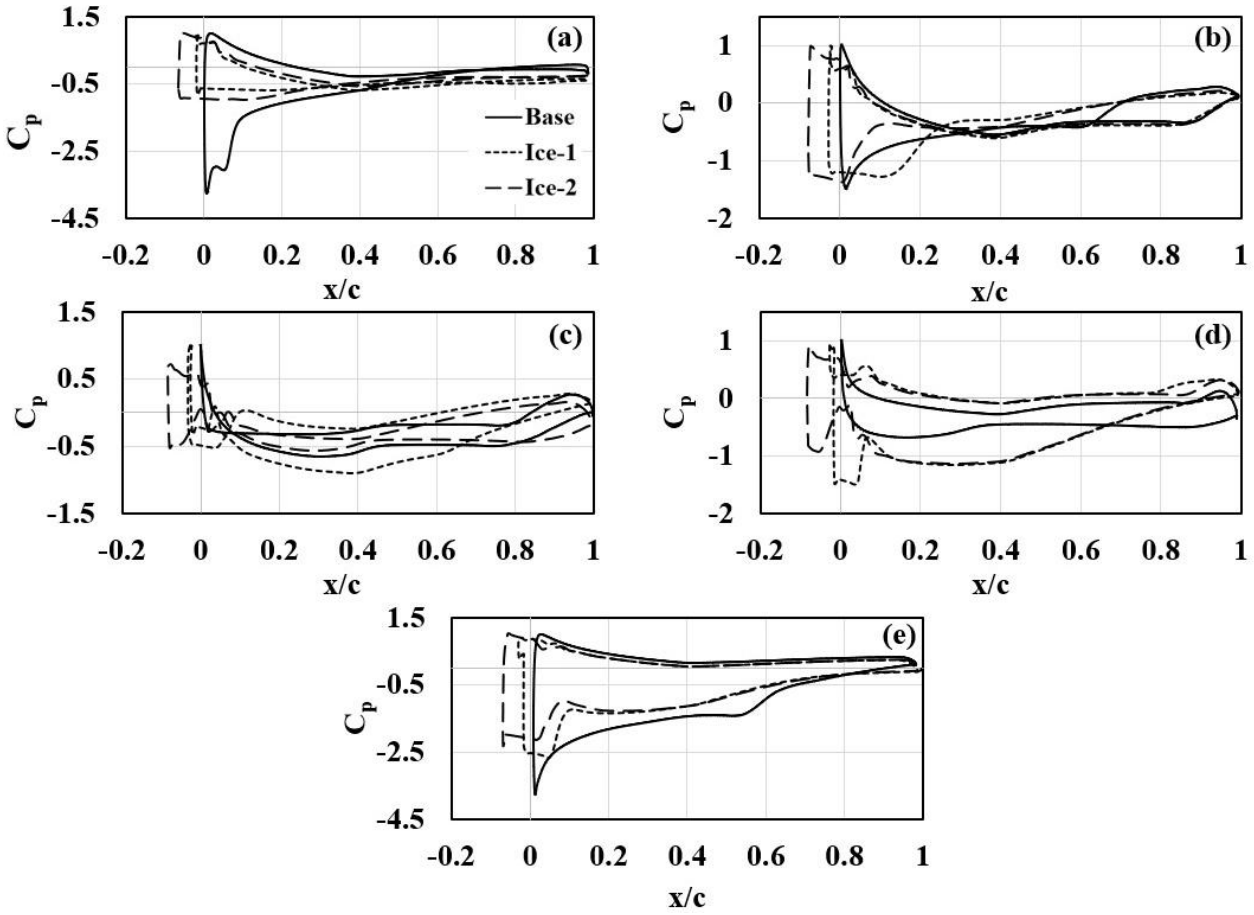

Figure 12: Pressure coefficient for Ice-1, Ice-2 and Base in (a) AoA= -10°, (b) AoA= -5°, (c) AoA= 0°, (d) AoA= 5°, (e) AoA= 10°.

Overall, Ice-1 and Ice-2 show different aerodynamic performance compared to Base specially in positive angles of attack. While both Ice-1 and Ice-2 experience an increase in lift coefficient with rising angle of attack, they exhibit lower aerodynamic performance at AoA=10° compared to Base, where Base performs optimally [40,41]. This is attributed to the presence of a separation region on the upper area of the airfoils in Ice-1 and Ice-2, which is absent in Base case. However, at AoA=5°, both Ice-1 and ice-2 have the best performance, and Base is performing weakly due to a separation region starting around x/c=0.4 on the upper side which increases the drag

coefficient while due to the separation bubbles on the upper side of Ice-1 and Ice-2, no separation happens. As a result, the best aerodynamic performance moved forward by 5° angle of attack.

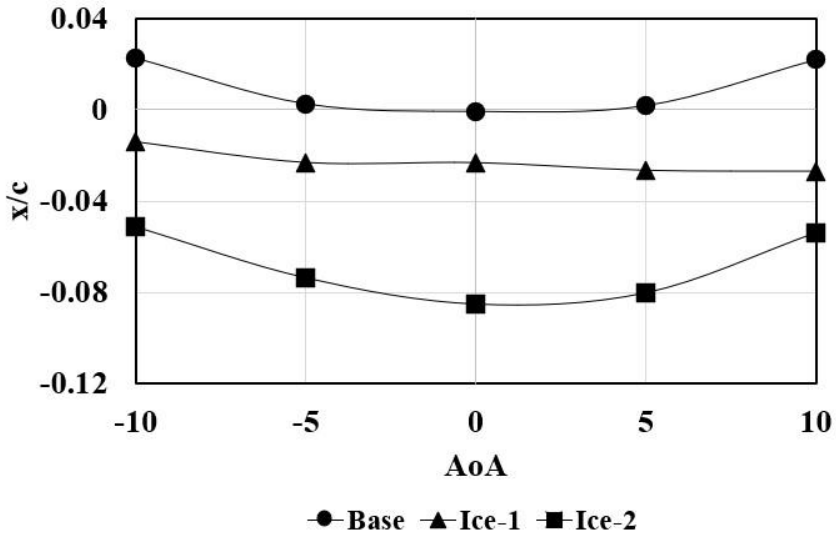

Figure 13: Stagnation point location for Base, Ice-1 and Ice-2.

The location of the stagnation point on an airfoil significantly influences pressure distribution and aerodynamic performance. When the stagnation point is positioned on the lower area, typically at a positive AoA and near the leading edge, it enhances suction on the upper surface, thereby generating lift. However, as the stagnation point shifts further downward, an adverse pressure gradient intensifies, leading to a reduction in lift efficiency. Conversely, if the stagnation point is on the upper surface, indicating a negative angle of attack, its upward movement increases the APG on the upper surface, potentially causing premature separation and a rise in drag. Figure 13 illustrates the stagnation point locations for Base, Ice-1, and Ice-2 across varying angles of attack. Considering Base, there is a symmetrical trend from negative to positive AoAs which happens because of the symmetrical shapes of the airfoil. At negative angles of attack, the stagnation point is positioned on the upper area of the airfoil, leading to a low-pressure region on the lower area. As the AoA increases, the stagnation point position shifts toward the leading edge, weakening the low-pressure region. At positive AOAs, the stagnation point relocates to the lower area, creating a low-pressure zone on the upper area of the airfoil, which enhances the lift coefficient.

The stagnation point position remains largely unchanged in the x-direction for Ice-1 and it changes mostly in the direction despite variations in AoA. At negative angles of attack, it is situated on the upper area of the airfoil right after the LE, forming a low-pressure distribution zone on the lower side, then the point shifts to the gap between the two horn structures of ice profile at AoA=0°, and moving to the lower surface at positive angles of attack. This causes the low-pressure distribution to happen on the upper side of the airfoil.

For Ice-2, the ice shape closely resembles the LE of the airfoil, resulting in the same trend for stagnation point position to Base but with an offset of d/c=0.08 where d represents the thickness of the ice on the leading edge. At negative AoAs, the stagnation point is located on the upper side of the airfoil, creating a low-pressure zone on the lower side. This leads to a negative lift for Ice-2. As the AoA increases, the stagnation point displaces toward the LE, weakening the low-pressure region on the upper side until, at AoA=0°, the stagnation point aligns with the LE, and the low-pressure region nearly disappears. With further increases in the AoA, the stagnation point position shifts to the lower surface, recreating a low-pressure region on the upper side. This enhances the lift coefficient because of the favourable pressure distribution.

3.1.2. Aerodynamic characteristics of Ice-3

The aerodynamic characteristics of Ice-3, a parametric ice profile, are analyzed in comparison to Base case as well as the experimental ice profiles Ice-1 (glaze) and Ice-2 (rime) across AoAs from -10° to 10°, as illustrated in Figure 14. As shown in Figure 14(a), the drag coefficient for Ice-3 fluctuates across different angles of attack but follows an overall increasing trend at positive angles. Meanwhile, the lift coefficient (Figure 14(b)) generally rises with the angle of attack, peaking around AoA = 5°, before beginning to decline. Regarding aerodynamic performance, Figure 14(c) shows that Ice-3 exhibits less variation compared to Base, Ice-1, and Ice-2. However, it reaches its maximum performance at AoA = 5°.

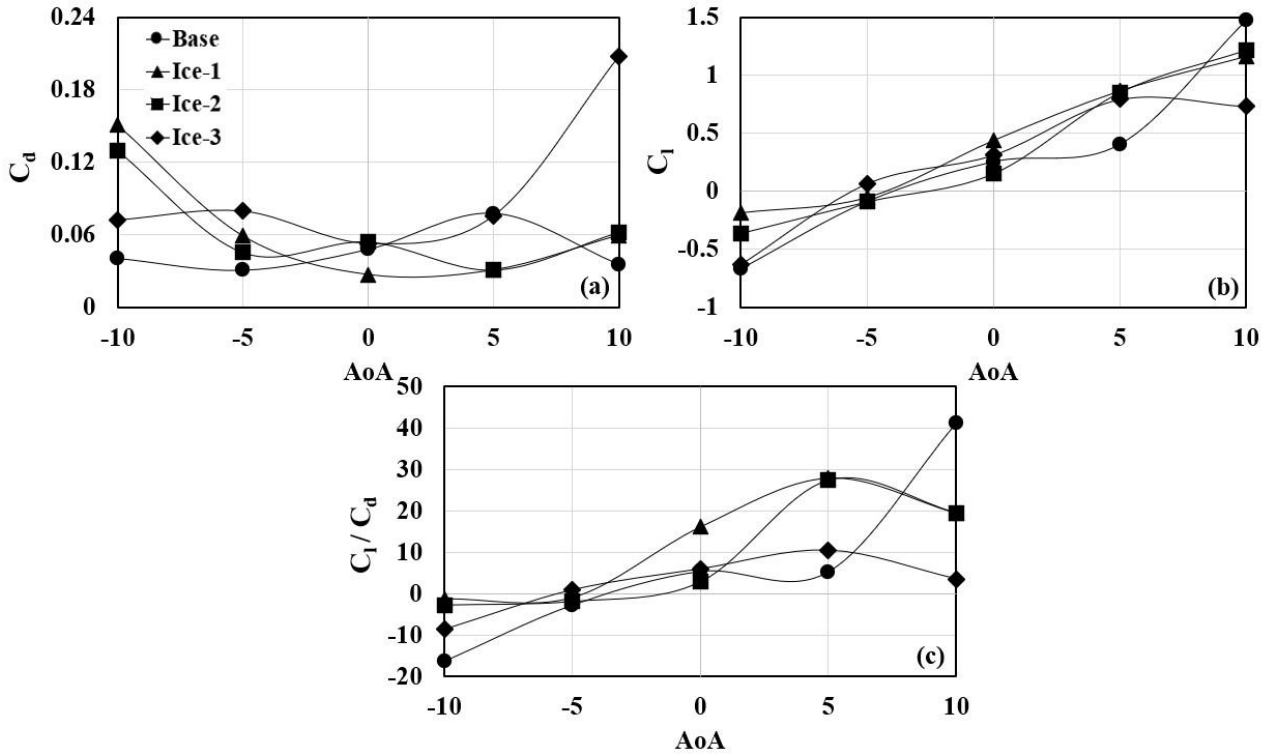

Figure 14: (a) Drag coefficient for Base, Ice-1, Ice-2 and Ice-3, (b) lift coefficient for Base, Ice-1, Ice-2 and Ice-3, (c) aerodynamic performance for Base, Ice-1, Ice-2 and Ice-3.

For Ice-3, the presence of ice creates an obstacle, particularly on the lower surface, significantly affecting flow behaviour at negative angles of attack. At these angles, ice-induced flow separation extends across the lower area to the TE, as illustrated by the velocity magnitude contour in Figure 15(a). This separation increases pressure drag, leading to a higher drag coefficient compared to Base case. As the AoA increases, the separation region on the lower side of Ice-3 intensifies due to the higher APG, as seen in Figure 15(b), resulting in a 157% higher drag coefficient than Base. However, at positive AoA, the separation region on the lower area transforms into a separation bubble, which reduces its impact on pressure drag. Meanwhile, on the upper area, a separation bubble begins to form near the LE due to the presence of ice. This bubble helps maintain attached flow over the airfoil, delaying stall. With a further increase in the AoA, a large separation zone develops on the upper surface due to the adverse pressure gradient, ultimately leading to stall and a significant drop in aerodynamic performance, as shown in Figure 10(e).

To explain the lift coefficient, the pressure coefficient is considered around Ice-3. In high negative angles of attack (Figure 16(a)), the pressure distribution around Ice-3 is similar to Base with some differences in the separation point, where the pressure coefficient has some jumps on the lower area. As the AoA increases, the behaviour of the pressure coefficient differs because of the greater separation region and the absence of the low-pressure zone on the lower area of Ice-3 resulting in less lift coefficient compared to Base. By increasing the AoA, in positive angles of attack, the separation bubble on the upper side of Ice-3 creating a constant pressure zone which extends from x/c=-0.1 to x/c=0.1 (Figure 16(c) and 11(d)) and by increasing the AoA, the difference between the pressure coefficient on two sides of the airfoil in Ice-3 gets more dominant which results in higher lift coefficient (in AoA=5° the lift coefficient is 95% higher compared to Base). After that, as the angle of attack increases, the airfoil faces the stall and loses the aerodynamic features resulting in a significant reduction in lift coefficient. Considering the aerodynamic performance of Ice-3 from Figure 14(c) it can be said that it has an ascending trend from negative to early positive angles of attack and it hits its maximum in AoA=5° which is 100% higher than Base and then it decreases with the increase in AoA.

To analyze the lift coefficient of Ice-3, the pressure coefficient distribution around the airfoil is examined (Figure 16). At high negative AoA (Figure 16(a)), the pressure distribution around Ice-3 is generally similar to Base case, with notable differences in the separation point, where a pressure coefficient jump is observed on the lower area. As the AoA increases, the pressure coefficient behavior changes due to the larger separation region and the absence of a strong low-pressure zone on the lower area of Ice-3. This results in less lift coefficient compared to Base. At positive AoA, a separation bubble initiates on the upper surface, creating a constant pressure zone extending from x/c = -0.1 to x/c = 0.1, as shown in Figure 16(c) and 11(d). With further increases in the AoA, the pressure difference between the lower and upper surfaces becomes more pronounced, leading to a higher lift coefficient. At AoA = 5°, the lift coefficient is 95% higher than Base. Beyond 5°, as the AoA continues to rise, stall happens to the airfoil, causing a loss of aerodynamic efficiency and a significant drop in lift coefficient. Examining the aerodynamic performance of Ice-3 in Figure 9(c), it follows an ascending trend from negative to early positive angles of attack, reaching its maximum at AoA = 5°, where it is 100% higher than

Base case. After this point, aerodynamic performance declines with increasing angle of attack due to increased drag and flow separation effects.

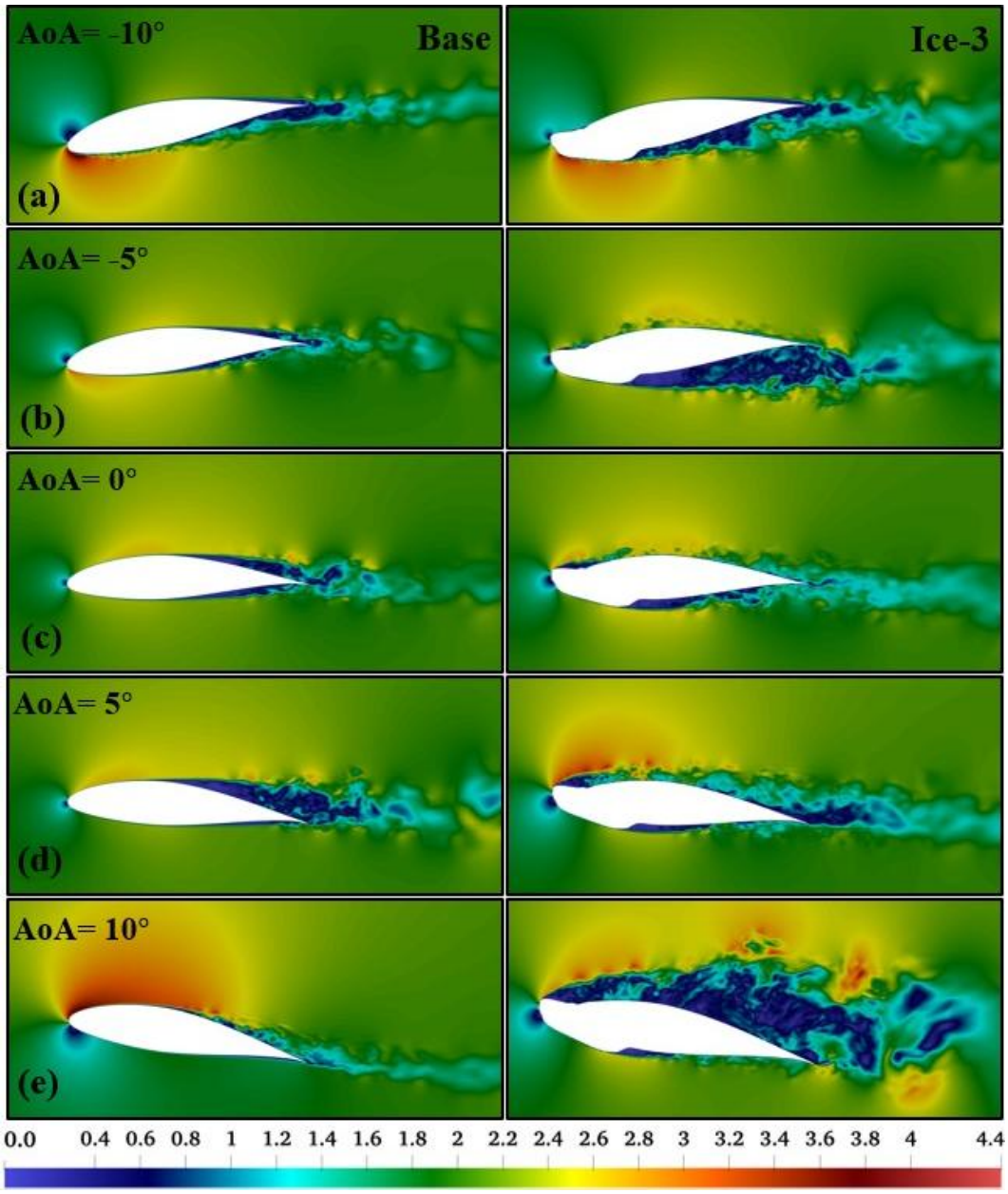

Figure 15: Velocity magnitude contour for Base and Ice-3 at (a) AoA= -10°, (b) AoA= -5°, (c) AoA= 0°, (d) AoA= 5°, (e) AoA= 10°

Comparisons between Ice-3 and Ice-1 demonstrate the impact of distinct ice profiles on aerodynamic performance. For Ice-3, the lift coefficient increases with the angle of attack up to AoA=5°, following a similar upward trend to Ice-1. However, the lift coefficient for Ice-3 fluctuates more than Ice-1 due to the ice on the lower side that extended more than Ice-1 and creates

separation. At high angles of attack, around AoA=10°, Ice-3 experiences stall on the upper surface, causing the lift coefficient to decrease by 237% compared to Ice-1. In terms of drag coefficient, except from high negative angles of attack, Ice-1 has a larger separation region on the upper area leading to a higher drag coefficient, both Ice-3 and Ice-1 follow similar trends from AoA=-5° to AoA=5°, with Ice-1 showing slightly lower drag due to absence of separation region on ant side of Ice-1. However, at AoA=10°, Ice-3 consistently shows a higher drag coefficient, about 246% greater because of the stall. The aerodynamic performance of both Ice-3 and Ice-1 increases till AoA=5° with an offset that shows Ice-1 is performing more efficiently (Figure 14(c)) because of the lower drag coefficient.

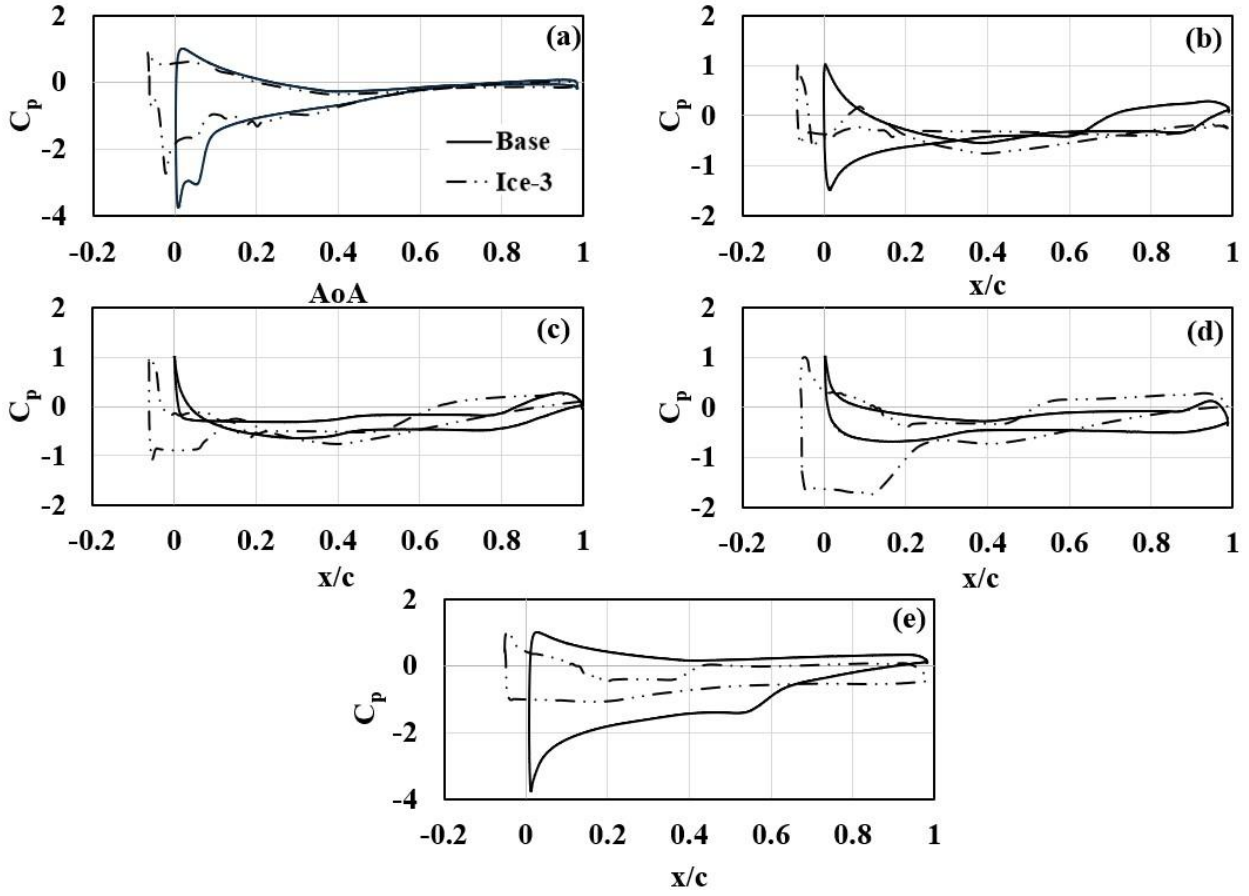

Figure 16: Pressure coefficient for Ice-3 and Base at (a) AoA= -10°, (b) AoA= -5°, (c) AoA=0°, (d) AoA=5°, (e) AoA=10°

A further comparison between Ice-3 and Ice-2 highlights differences in aerodynamic characteristics. The shape of Ice-2 remains closer to Base, so the differences between Ice-3 and Ice-2 resemble those observed between Ice-3 and Base. For Ice-2, the lift coefficient increases

consistently with the AoA. By comparing the lift coefficients of Ice-3 and Ice-2, the same increasing trend is followed by the two cases till Ice-3 faces the stall and the lift coefficient decreases, but the lift coefficient in Ice-2 continues to increase by increasing the AoA increases up to 10 degrees. Regarding the drag coefficient, Ice-3 follows a different trend compared to Ice-2. From AoA=-10° to AoA=-5°, the drag coefficient of Ice-2 decreases as the separation boundary layer weakens on the lower side of Ice-2, while it strengthens in Ice-3. From AoA=-5° to AoA=0°, the drag coefficient increases in Ice-2 because of the development of a separation region on the upper area, whereas in Ice-3, the separation on the lower surface diminishes. Between AoA=0° and AoA=5°, the drag coefficient of Ice-2 decreases as the stays attached to the airfoil, while in Ice-3, separation gets more dominant on the upper surface, increasing pressure drag. For both cases, the drag coefficient increases from AoA=5° to AoA=10° due to the development of separation on the upper area of the airfoils. Although, the increase in drag coefficient in Ice-3 is more dominant because of the stall.

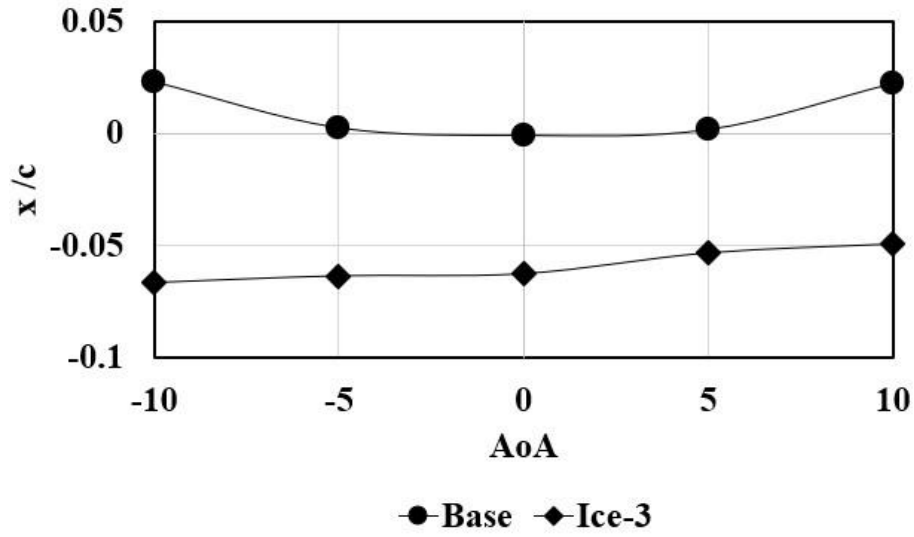

Figure 17: Stagnation point position for Base and Ice-3

Figure 17 presents the stagnation point location for both Base and Ice-3. The stagnation point location for Base case was discussed in Section 1.4. For Ice-3, the stagnation point position is not as symmetrical as Base. It begins at the LE of the iced airfoil and because of the specific ice shape, the point does not change significantly in the x-direction, and it mostly dislocates in the y-direction from negative to positive angles of attack. Unlike Base case, in negative angles of attack,

the stagnation point position does not shift to the upper area. At high negative angles of attack (AoA=-10°), a significant low-pressure zone forms on the lower area of the airfoil combined with the effect of ice geometry on the lower side, leads to separation on the lower area. As the AoA increases, the stagnation point gradually moves toward the lower side. This shift causes the low-pressure zone on the lower surface to diminish. With further increases in the angle of attack, the stagnation point moves forward to the lower side, weakening the separation on the lower side while generating a small low-pressure region on the upper area that expands gradually. This behaviour shows that as the stagnation point moves toward one side of the airfoil, separation decreases on that side. Conversely, separation forms on the opposite side of the stagnation point, influenced by the interaction between stagnation point dynamics and ice-induced geometry changes.

4. Results and Discussion: Flow Structure Analysis

4.1. Overview

The initial phase of this study investigated the impact of two experimental ice profiles (Ice-1 and Ice-2) and one parametric profile (Ice-3) on the aerodynamic characteristics of an airfoil. The findings indicated significant degradation in performance due to ice accretion, which adversely affected both the boundary layer behavior and overall aerodynamic efficiency. Specifically, at an angle of attack (AoA) of 10°, the condition under which the clean airfoil exhibits peak performance, a reduction of 52% in aerodynamic performance was observed for Ice-1 and Ice-2, while Ice-3 experienced a stall condition.

In the present chapter, the focus is directed toward a detailed flow structure analysis of the two experimental ice profiles (Ice-1 and Ice-2) at an AoA of 10°, with comparisons made to the clean airfoil. Instantaneous flow field data, extracted at the final time step (30^{th} second) from LES results, acts as the basis for this analysis. In the first part of the results, flow structures are visualized through iso-surfaces of the second invariant of the velocity gradient tensor (Q-criterion) and velocity contours. The positions of separation points and the formation of separation bubbles on the iced airfoils are identified and contrasted with those observed on the clean airfoil, using friction coefficient analysis as the evaluative metric. The second section presents an assessment of turbulent kinetic energy (TKE) across the iced airfoils, with direct comparisons drawn to the clean model. Furthermore, fluctuations in the three principal directions, represented by the components of the Reynolds stress tensor, are examined to elucidate the relationship between the flow structures and these fluctuations.

4.1.1. Flow Structure Visualization

Figure 14 presents the time-averaged streamwise velocity contours, along with the streamlines, for the three analyzed cases: Base, Ice-1, and Ice-2. These velocity contours provide insight into the effect of ice accretion on flow separation and aerodynamic performance. In Base case, as shown in Figure 14(a), the flow remains largely attached along the suction side of the airfoil due to the favorable pressure gradient in the early stages. However, a thin separation bubble forms between x/c = 0.55 and x/c = 0.65 due to the adverse pressure gradient. This

indicates a minor disturbance in the flow, which quickly reattaches downstream, allowing the airfoil to maintain relatively high aerodynamic performance.

In contrast, Figure 14(b) illustrates the velocity distribution for Ice-1 case, where the presence of ice on the leading edge significantly alters the flow characteristics. The ice formation induces an earlier separation, with a separation bubble forming from x/c = -0.015 to x/c = 0.11. This premature flow detachment is due to the abrupt changes in airfoil geometry introduced by ice accretion. Additionally, a secondary separation region occurs near the trailing edge, around x/c = 0.9 and the end of the airfoil, caused by an intensified adverse pressure gradient. The extended flow separation reduces aerodynamic efficiency, leading to a decline in lift generation and increased drag.

Similarly, Figure 14(c) demonstrates Ice-2 case, where the presence of ice at the leading edge leads to the formation of a separation bubble from x/c = -0.04 to x/c = 0.1. This suggests a slightly larger region of early separation compared to Ice-1, indicating that the specific shape and extent of ice accretion significantly influence boundary layer behavior. However, towards the trailing edge, a relatively smaller separation region is observed at approximately x/c = 0.95, compared to Ice-1. The reduced separation at the trailing edge suggests that while the leading-edge ice disrupts the initial flow attachment, the trailing-edge effects vary depending on the ice profile.

A common feature across all three cases is the presence of a high-velocity region on the suction side in the early section of the airfoil. This region contributes to maintaining attached flow initially, despite the presence of ice. However, as the flow progresses downstream, the interaction between the boundary layer and the adverse pressure gradient dictates the extent of separation. The findings indicate that the presence of ice significantly impacts flow attachment, separation dynamics, and ultimately, aerodynamic efficiency.

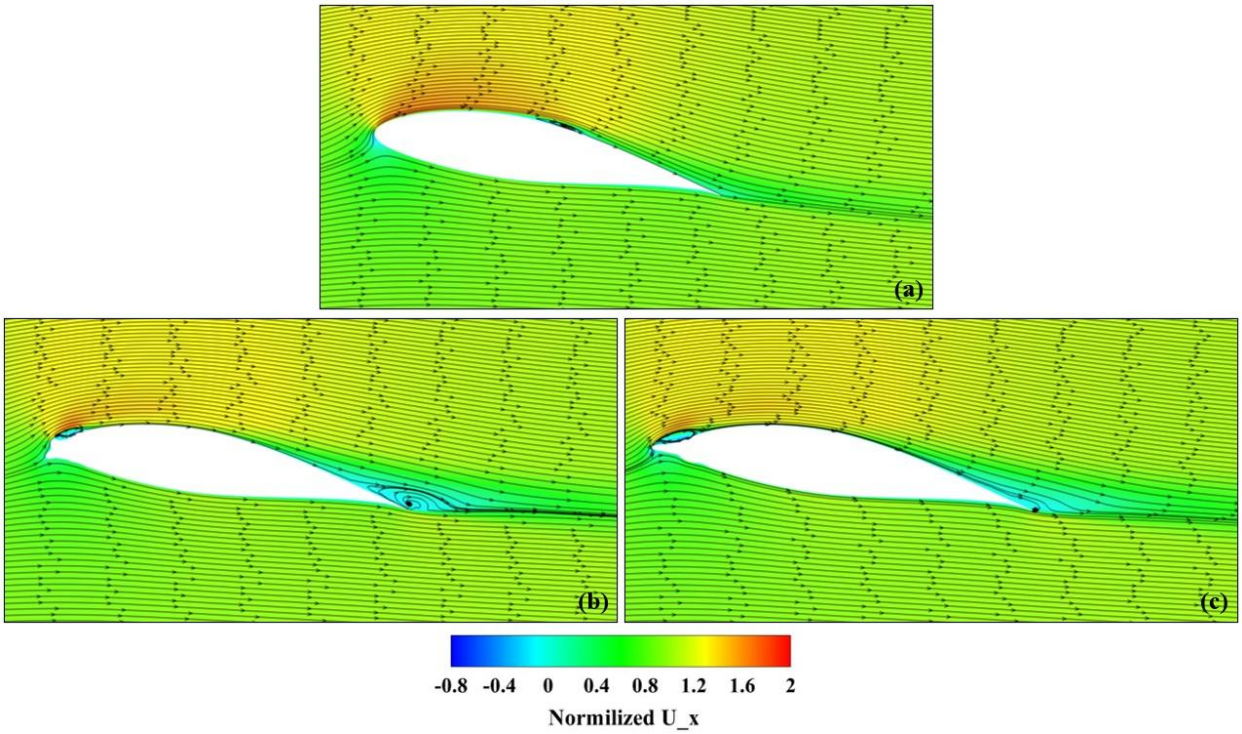

Figure 18: Contour of time-averaged streamwise velocity and streamlines for (a) Base, (b) Ice-1, (c) Ice-2.

The location of the separation and reattachment points on the suction side of an airfoil is critically important because they play a critical role in determining the overall aerodynamic performance. These points dictate the extent and behavior of the boundary layer, which in turn affects key performance parameters such as lift, drag, and stall characteristics. In particular, the suction side is responsible for generating lift through the creation of a low-pressure region. The precise locations where the flow detaches and reattaches have a direct impact on the pressure distribution along the airfoil surface [45,46]. Any shift in these points, especially due to external factors like ice accretion, can alter the effective camber of the airfoil and consequently its lift production.

Moreover, in terms of iced airfoils, the alteration of these critical points can be considered as a tool for assessing performance degradation. Changes in the separation and reattachment locations can indicate how the ice impacts the boundary layer behavior, providing insights into the aerodynamic penalties imposed by ice accretion.

To gain a deeper understanding of the precise locations of flow separation and reattachment, this study examines the normalized wall shear stress, which is quantified as the friction coefficient (C_f) in the streamwise direction, along the suction side of the airfoil at the midspan plane (refer to Figure 19). In parallel, Figure 20 presents the instantaneous velocity contours for the three cases at the 30th second, the final time step of the simulation, offering a detailed snapshot of the flow field at that moment. The friction coefficient (C_f) is a parameter in order to show the state of the boundary layer along the airfoil. Specifically, when C_f takes negative values, it signifies that the flow is separating from the surface. Conversely, a value of zero ($C_f = 0$) indicates the location where the flow is either in the process of separating or reattaching, conditioned by the flow behavior [45,46]. The friction coefficient is crucial for identifying the dynamic behavior of the boundary layer, especially in regions influenced by adverse pressure gradients.

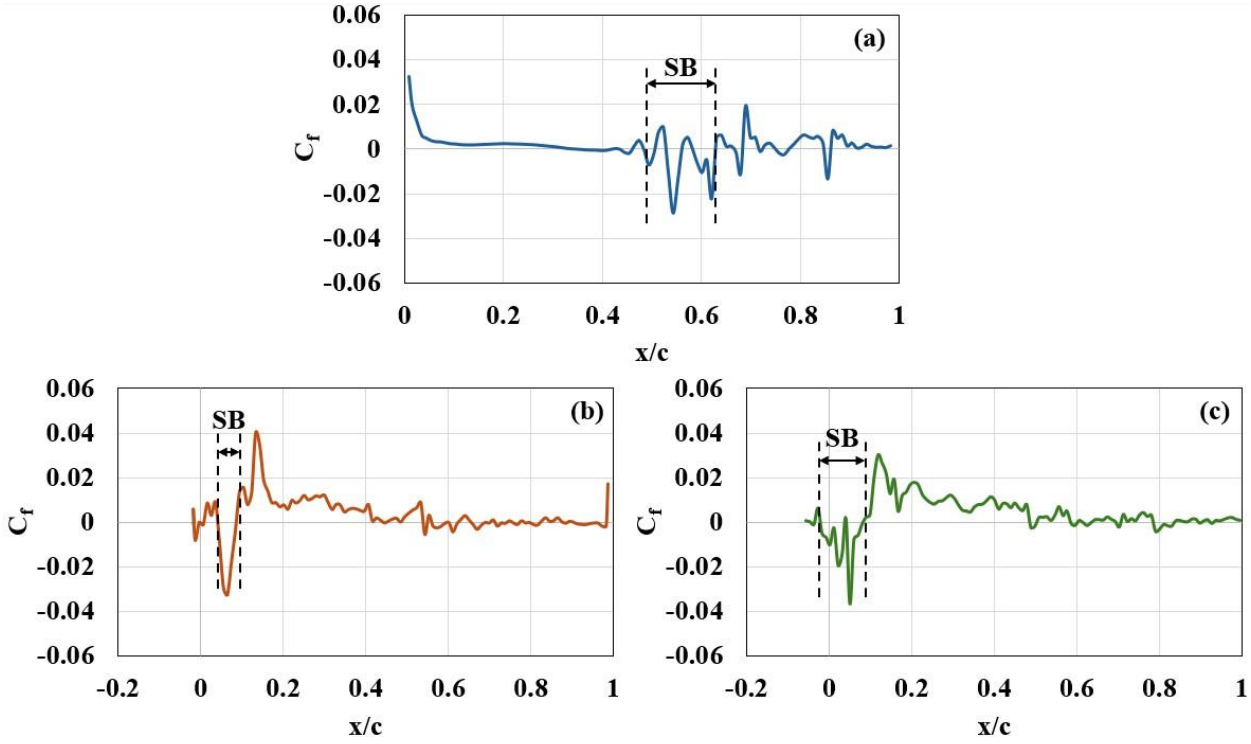

Figure 19: Friction coefficient in x-direction on the suction side of the airfoil for (a) Bsse, (b) Ice-1, (c) Ice-2.

In Base scenario depicted in Figure 19(a), the analysis shows that the flow remains fully attached to the airfoil up to a chordwise position of approximately x/c=0.42. Beyond this point,

the friction coefficient begins to fluctuate, indicating the initiation of flow separation. These fluctuations reveal a region where the flow detaches and reattaches periodically, which is shown as a separation bubble spanning roughly from x/c=0.5 to x/c=0.65. This observed separation bubble aligns with the thin separation region visible in the instantaneous velocity contours in Figure 20(a). Furthermore, as the flow continues along the suction side towards the trailing edge, the interplay between the local pressure gradients and boundary layer dynamics becomes increasingly complex. The data indicate that small separation bubbles are continuously generated and dissipated, a process that persists along the remainder of the airfoil. This cyclic creation and destruction of separation bubbles underscore the dynamic nature of the flow, where local disturbances and pressure fluctuations govern the attachment and detachment processes.

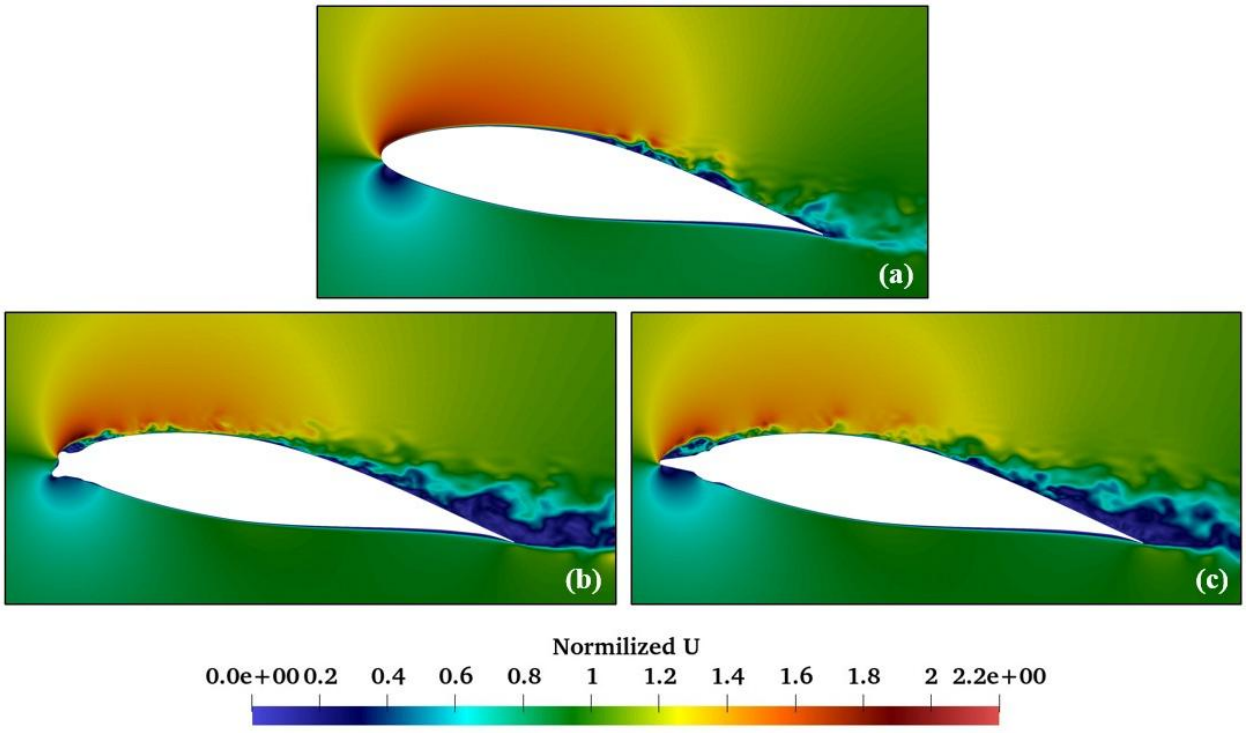

Figure 20: Instantaneous velocity contour in mid-span plane for (a) Base, (b) Ice-1, (c) Ice-2.

Figure 19(b) presents the friction coefficient (C_f) for Ice-1, clearly illustrating an early-stage separation bubble where C_f has negative values, starting approximately from x/c=-0.05 to x/c=0.05. This negative C_f region indicates that the flow initially separates from the airfoil surface. Beyond this early separation, the flow reattaches, as evidenced by the shift to positive

C_f values around x/c=0.55. However, further downstream, the friction coefficient exhibits fluctuating behavior that continues to the trailing edge, reflecting irregular separation and reattachment phenomena. Correspondingly, Figure 20(b) confirms these findings by showing that the flow separates around x/c=0.55, accompanied by small reattachment zones that maintain C_f values close to zero in that region.

In Figure 19(c), which illustrates C_f for Ice-2 case, a separation bubble is similarly observed on the suction side of the airfoil. This observation agrees with the streamline patterns depicted in Figure 18(c). After this initial separation bubble, the flow remains fully attached to the surface until approximately x/c=0.5, where the friction coefficient becomes consistently positive. Beyond this point, the fluctuations in C_f resume, extending towards the trailing edge, indicating renewed separation events. Figure 20(c) further confirms the presence of an early-stage separation bubble for Ice-2, followed by an extended region of attached flow that results in positive C_f values, and subsequently a zone of separation beginning around x/c=0.5.

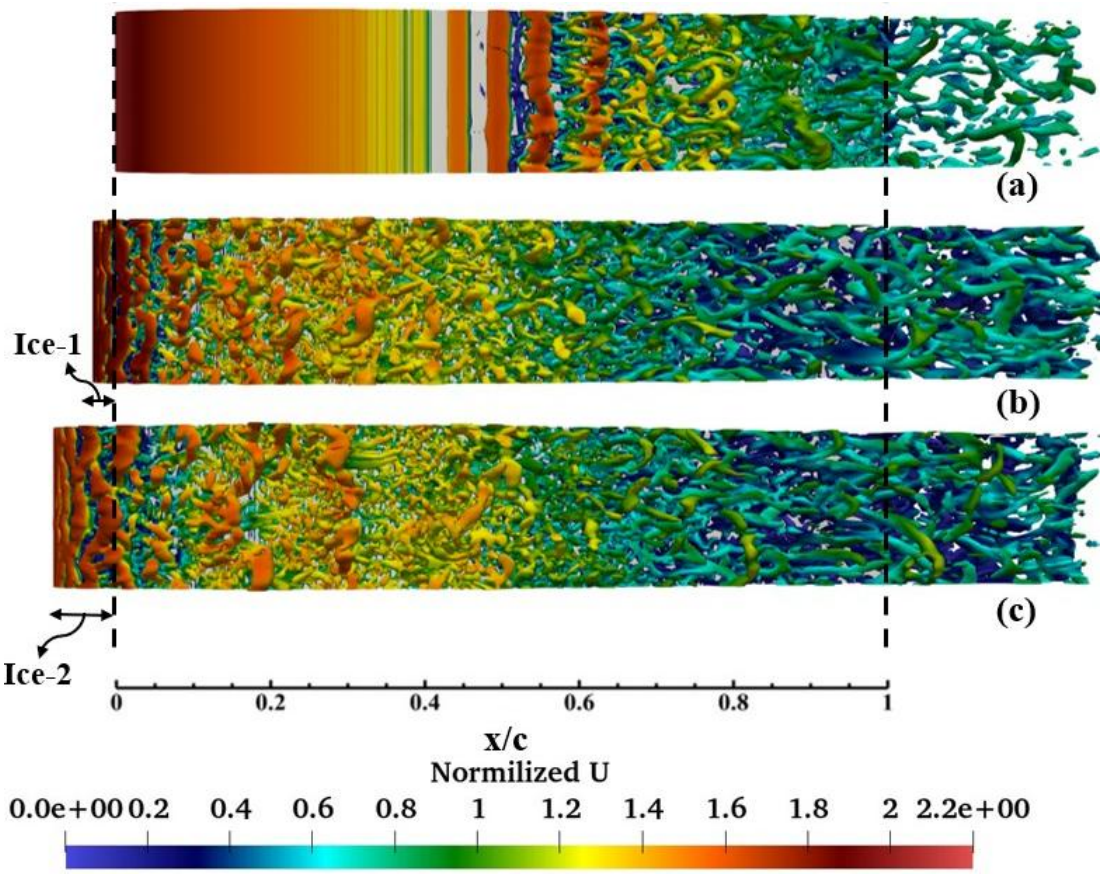

Figure 21: Top view of instantaneous Q-criterion iso-surfaces ($Q = 150\,U^2/c^2$) colored by velocity field (a) Base, (b) Ice-1 and (c) Ice-2.

One of the most effective methods for visualizing coherent flow structures over an airfoil is the use of the Q-criterion, which is based on the second invariant of the velocity gradient tensor, as introduced by Hunt et al. [26]. This technique is important in analyzing the emergence, interaction, and evolution of coherent structures, as well as in capturing the wake formation process on the suction side of the airfoil. Essentially, the Q-criterion designates a region as vortical if it meets a specific mathematical condition, thereby allowing for the detailed identification and study of vortices within the complex flow field [47–49].

$$Q = \frac{1}{2}\left(|\Omega|^2 - |S|^2\right) > 0 \tag{13}$$

Where S is the rate of strain tensor and Ω is the vorticity tensor. The definitions are as follows [47,48].

$$S = \frac{1}{2}\left(\nabla u + \nabla u^T\right) \tag{14}$$

$$\Omega = \frac{1}{2}\left(\nabla u - \nabla u^T\right) \tag{15}$$

The instantaneous Q-criterion iso-surfaces, illustrated in Figure 21 and colored by normalized velocity magnitude, provide a detailed visualization of the evolving flow structures on the suction side of the airfoil. As shown in Figure 21(a), laminar flow separates from the surface at approximately x/c=0.4, initiating the formation of two-dimensional Kelvin–Helmholtz (K-H) vortices due to shear layer instabilities [50–54]. These vortices, driven by K-H instability mechanisms [42,51,55–57], persist as they convect downstream. By x/c=0.6, the initially two-dimensional vortical structures transition into three-dimensional formations, predominantly in the form of hairpin vortices [55,58,59], which further expand toward the trailing edge. Figure 22 presents an isometric view of the Q-criterion iso-surfaces, offering additional insight into the evolution of coherent flow structures in Base. Near the leading edge, the flow remains laminar and fully attached. However, as the flow moves downstream, laminar separation initiates at approximately x/c=0.4, leading to the development of organized 2D K-H vortices, characteristic of shear layer instabilities as was mentioned. Initially, these vortices are well-structured and confined near the airfoil surface. As instability intensifies, secondary instabilities cause these

vortices to break down into three-dimensional structures. Around x/c=0.6, this transition becomes well-defined, with hairpin vortices emerging as the dominant structures [58]. These vortices play a crucial role in enhancing turbulent momentum transfer [60], increasing mixing and energy cascade within the separated region. Further downstream, at x/c=0.8, larger-scale hairpin vortices develop, accompanied by increased vortex stretching and deformation [61]. At this stage, the initially well-organized coherent structures begin to lose periodicity, leading to a fully turbulent wake region. As turbulence intensity increases, streamwise-oriented vortices become more pronounced as they detach from the airfoil surface and transition into the wake. This evolution aligns with established findings on boundary layer transition and wake dynamics [62,63].

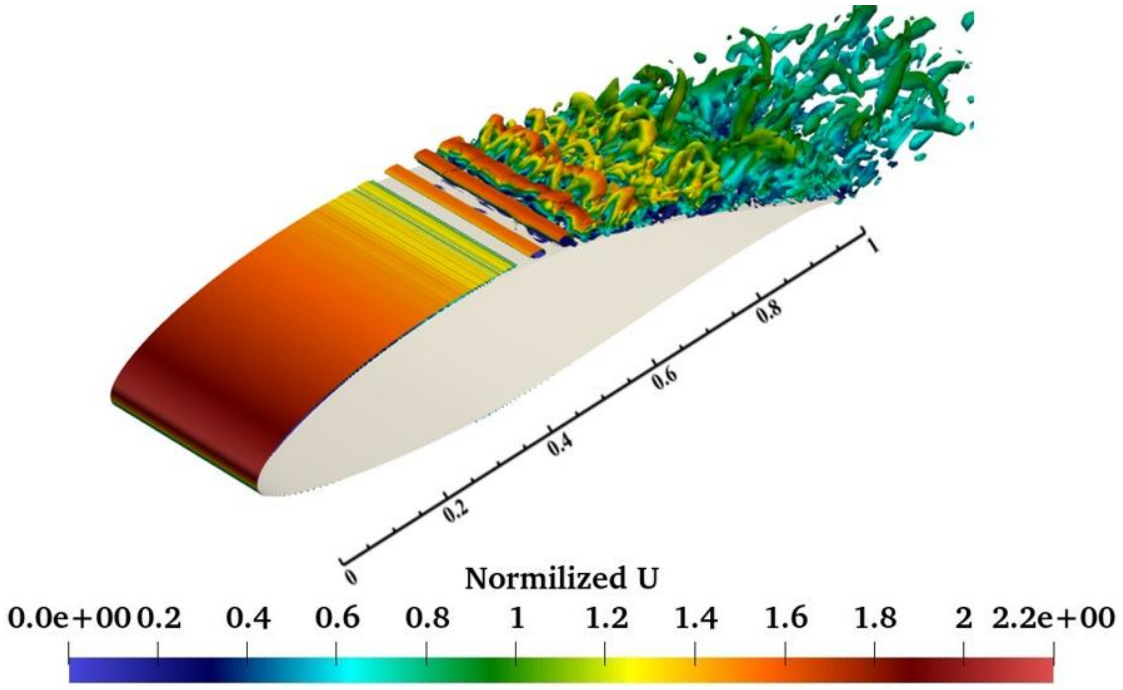

Figure 22: Isometric view of instantaneous Q-criterion iso-surfaces colored by velocity field for Base

Examining Figure 21(b), the presence of ice on Ice-1 shifts the start of K-H rolls closer to the leading edge, with these structures subsequently breaking down into hairpin and other three-dimensional vortices between x/c=0.1 and x/c=0.45. Compared to Base case, the vortical rolls in Ice-1 exhibit a more rapid breakdown into 3D structures and a higher velocity. As a result, these vortices are thinner and propagate faster downstream, showing an accelerated transition to turbulence. This phenomenon can be attributed to the ice acting as a geometric perturbation,

energizing and destabilizing the boundary layer at an earlier stage [61]. Figure 23 further illustrates the instantaneous Q-criterion iso-surfaces, capturing the evolution of coherent vortical structures over the suction side of Ice-1. When compared to Base case (Figure 22), the ice significantly alters the transition process, impacting the development, spatial arrangement, and intensity of turbulent structures. In Base case, the transition to turbulence follows the classical K-H instability mechanism, where spanwise vortices roll up, face breakdown, and eventually develop into organized hairpin structures. However, in Ice-1, ice profile causes this transition, resulting in a more disordered and less periodic arrangement of hairpin vortices.

The primary instability mechanism in Ice-1 differs from Base due to localized acceleration and deceleration induced by ice profile. These disturbances contribute to premature flow separation, enhancing secondary instabilities and expediting vortex roll-up and breakdown. As a result, coherent structures emerge earlier and exhibit a lower degree of spatial organization than in Base. Between x/c=0.2 and x/c=0.6, the flow remains largely attached to the suction surface, with hairpin vortices as the dominant structures. However, unlike Base, where these vortices form in a structured sequence and grow consistently in size downstream, those in Ice-1 appear more break down and irregular. This suggests that the ice profile disrupts the coherent development of hairpin vortices, likely due to increased momentum loss and enhanced turbulence production near the wall [64].

Beyond x/c=0.6, vortices begin to detach from the airfoil surface, forming the wake turbulence. However, their proximity to the suction surface remains closer than in Base, indicating that the ice profile reduces the penetration depth of turbulent structures into the outer flow. This modification in turbulent energy distribution suggests that energy remains more concentrated near the wall rather than being transferred into the freestream [25]. Additionally, the velocity distribution within these turbulent structures differs from Base. As the flow progresses downstream, the local velocity inside the vortical structures decreases, implying weaker momentum exchange between the boundary layer and the outer flow. This can be attributed to increased turbulence dissipation in the presence of ice, which weakens streamwise vortices and reduces overall momentum transport efficiency [62,65].

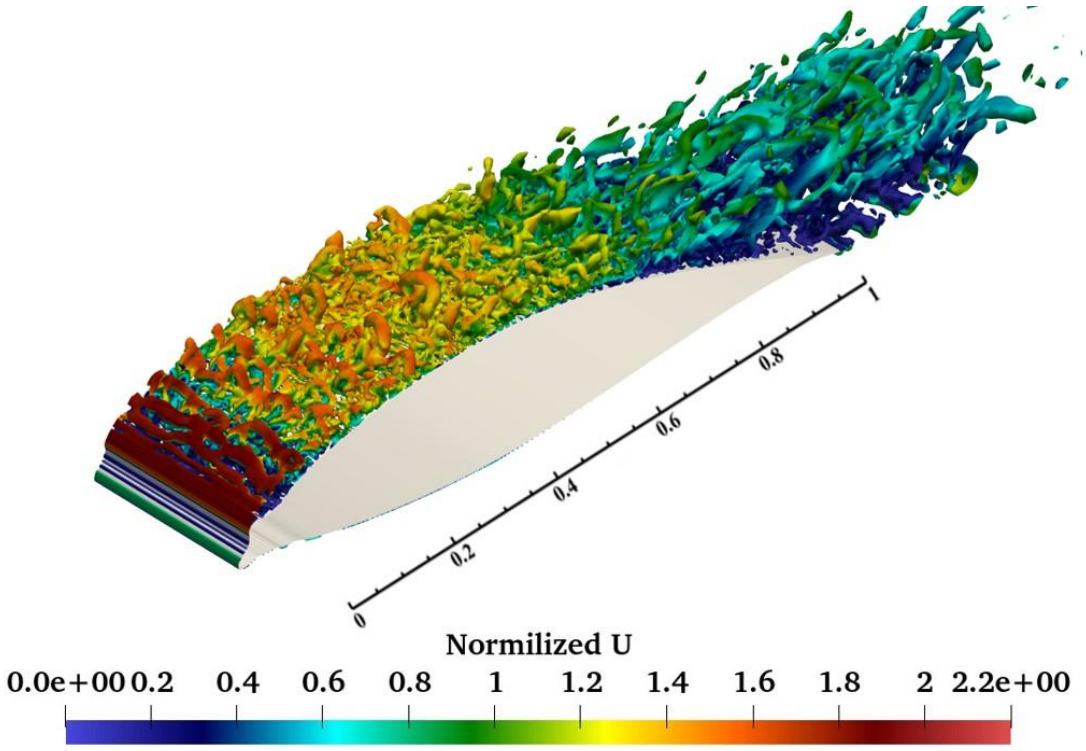

Figure 23: Isometric view of instantaneous Q-criterion iso-surfaces colored by velocity field for Ice-1

Ice-2 scenario (Figure 21(c)) presents a similar but more pronounced effect of ice accretion on transition dynamics. Initially, 2D K-H rolls form at the leading edge due to ice-induced shear layer instability [51]. These structures rapidly evolve into 3D vortices between x/c=0.1 and x/c=0.55, with higher velocity levels in the early transition stages compared to Base. However, as the structures moves to downstream, their velocity gradually decreases, leading to the formation of larger, stronger flow structures near the trailing edge and within the wake. Figure 24 illustrates the vortical structures over the suction side of Ice-2. The presence of ice disrupts the attached boundary layer, causing a sequence of flow phenomena that significantly alter aerodynamic performance. Immediately downstream of the ice, a sharp velocity gradient between the decelerated near-wall flow and the freestream initiates shear layer instability. This instability leads to the formation of periodic vortex rolls via the K-H mechanism, which rapidly develop into coherent hairpin vortices. These structures are intensified by the ice geometry, forcing an earlier transition to turbulence compared to Base.

As the flow progresses, hairpin vortices remain relatively stable over the mid-chord region (0<x/c<0.50), maintaining a turbulent boundary layer. However, beyond x/c=0.5, adverse pressure gradient effects and turbulent energy dissipation result in continuous flow deceleration. By x/c=0.7, the boundary layer loses momentum, leading to flow separation. The post-separation region is marked by the breakdown of coherent vortices into larger, more chaotic motions, which grow in scale and lose periodicity as they merge into a broad, unsteady wake [63,66]. Notably, the delayed full separation in Ice-2 suggests that ice-induced turbulence can sustain boundary layer attachment longer than in Base.

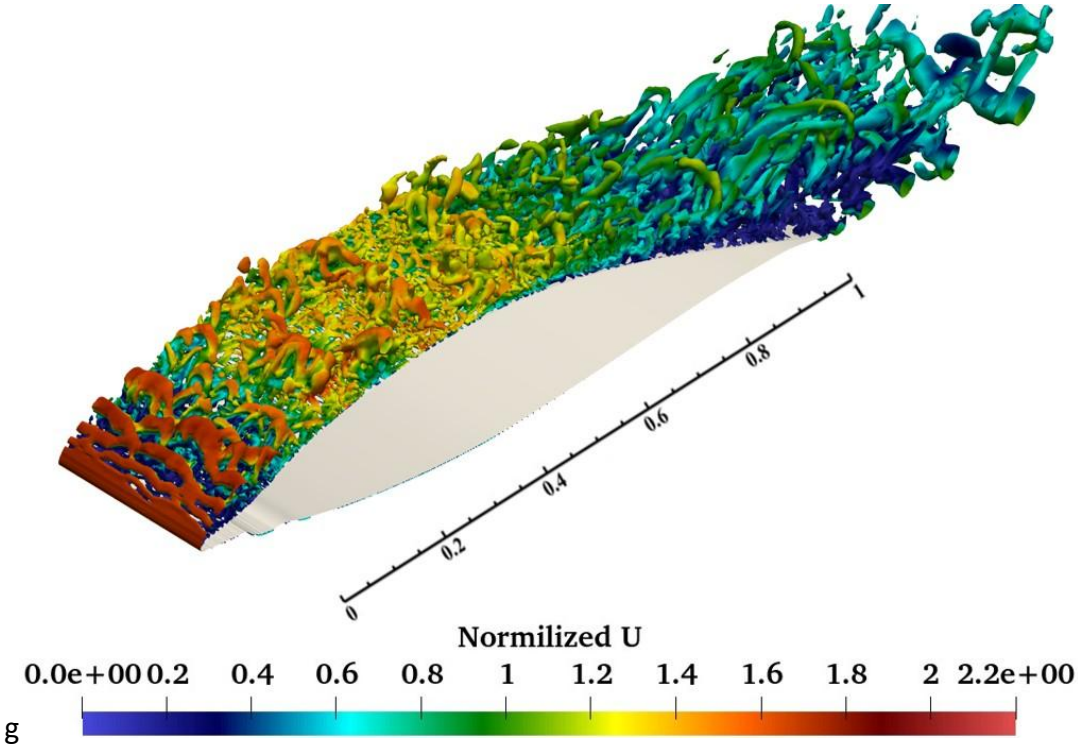

Figure 24: Isometric view of instantaneous Q-criterion iso-surfaces colored by velocity field for Ice-2

Both Ice-1 and Ice-2 reveal that ice accretion significantly changes the transition process by amplifying instability, accelerating vortex breakdown, and increasing turbulence intensity. While both cases exhibit early transition, Ice-2 features larger, more persistent turbulent structures near the trailing edge. In contrast, Ice-1 shows a more chaotic and less periodic arrangement of hairpin vortices, with stronger near-wall turbulence dissipation. These

differences emphasize the role of ice geometry in shaping the aerodynamic response of the airfoil.

4.1.2. Reynolds Stress Tensor

Turbulent Kinetic Energy (TKE) represents the energy contained within the turbulent eddies of a flow. In Large Eddy Simulation (LES), the resolved TKE (k_{res}) corresponds to the portion of this energy that is explicitly captured by the computational grid, primarily surrounding the larger, energy-containing eddies (The filter and grid are refined enough to resolve 80% of the energy at all locations [25,29,31,67]). Meanwhile, subgrid-scale (SGS) TKE (k_{SGS}) accounts for the energy associated with smaller eddies that are not directly resolved by the computational grid and instead require modeling. These subgrid scales play a crucial role in representing the dissipative processes occurring at scales below the grid resolution [30,32,68]. Consequently, the total turbulent kinetic energy can be determined using Eq. 16.

$$TKE = k_{res} + k_{SGS} \tag{16}$$

Where k_{res} calculates from Eq.17.

$$k_{res} = \frac{1}{2}(u'^2 + v'^2 + w'^2) \tag{17}$$

Figure 25 illustrates the normalized subgrid turbulent kinetic energy for three cases: Base, Ice-1, and Ice-2. In Figure 25(a), the subgrid scale TKE peaks between x/c=0.6 and x/c=0.8, which aligns with the region where 2D structures transition into hairpin structures, continuing up to x/c= 0.8 (Figure 22), with some energy being dissipated in the process. In Figure 25(b), for Ice-1, it can be observed that the SGS turbulent kinetic energy increases at the separation bubble near the leading edge, becoming more pronounced compared to Base. Since k_{SGS} represents the energy dissipated from the flow, this suggests that energy dissipation is greater in the separation bubble of Ice-1 than in Base case, as the separation bubble in Ice-1 results from ice accumulation, whereas in Base, it occurs due to the adverse pressure gradient. A similar interpretation can be made for Ice-2 in Figure 25(c) compared to Base.

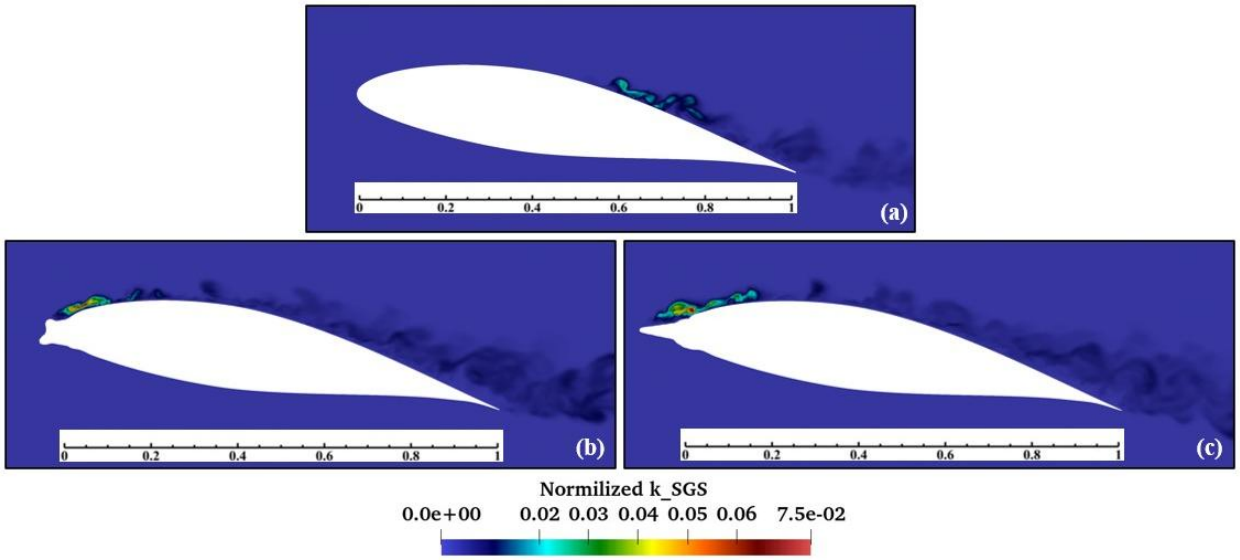

Figure 25: Subgrid scale turbulent kinetic energy for (a) Base, (b) Ice-1, (c) Ice-2.

Figure 26 presents the total turbulent kinetic energy for three different cases. The location where the TKE reaches its maximum corresponds to the region where the 3D hairpin vortex is formed by the breakdown of 2D rolls. One notable observation is the difference between the resolved TKE and the subgrid-scale TKE, with the resolved TKE being approximately two orders of magnitude higher. This highlights the accuracy of the LES simulation conducted in this study. As seen in Figure 26(a), the total TKE intensity is higher in comparison to Figure 26(b) and Figure 26(c), which represent Ice-1 and Ice-2, respectively. Taking into account the separation bubble thickness shown in Figure 18, the separation bubble for Base is thinner than those for Ice-1 and Ice-2, resulting in higher turbulence kinetic energy. Furthermore, due to the transition from 2D rolls to 3D structures and the continued growth of these structures, the TKE is higher for Base than for Ice-1 and Ice-2, where the structures remain relatively the same size after the separation bubble.

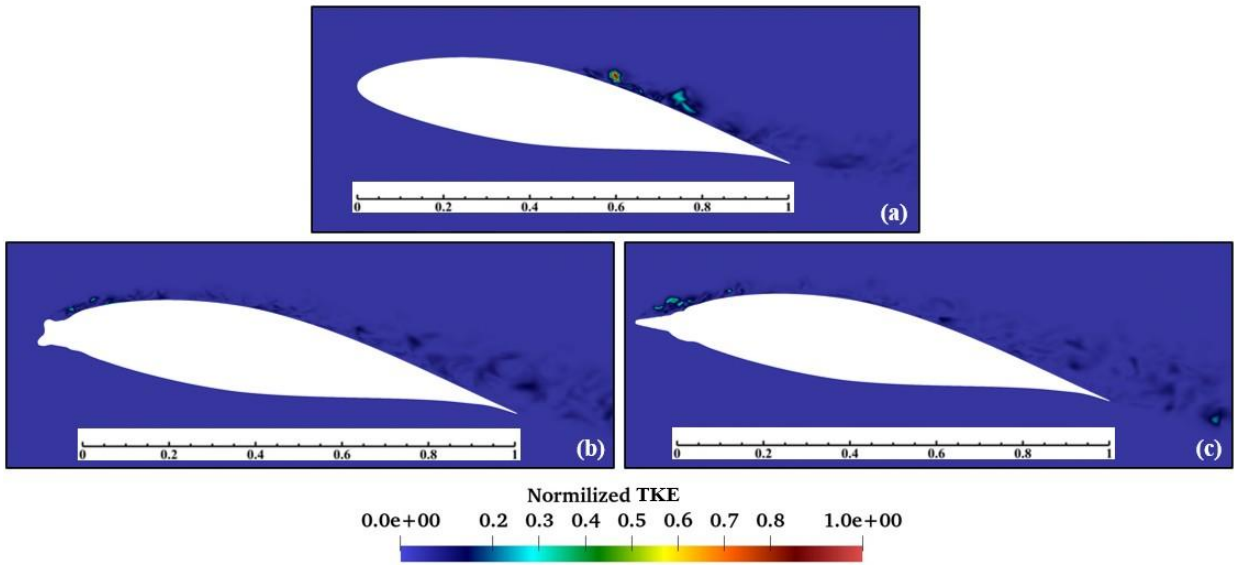

Figure 26: Turbulent kinetic energy for (a) Base, (b) Ice-1, (c) Ice-2.

Figure 27 and Figure 28 present the normalized streamwise and crosswise Reynolds normal stresses at three distinct x/c positions, respectively, representing different distances from the suction surface in y-direction. It is essential to note that Reynolds normal shear stresses are components of turbulent kinetic energy. In Figure 27(a) and Figure 28(a), which illustrate the fluctuation distribution at x/c=0.05, Base exhibits minimal fluctuation when compared to Ice-1 and Ice-2. This is attributed to the formation of separation bubbles around x/c=0.05 in both Ice-1 and Ice-2, leading to considerable fluctuations in these cases. For Ice-1, as the distance from the surface increases, both streamwise and crosswise fluctuations become more pronounced. However, these fluctuations attenuate shortly thereafter (at approximately y/c=0.02). In the case of streamwise fluctuations for Ice-1, two distinct peaks are observed at y/c=0.005 and y/c=0.007, whereas only one peak is evident for crosswise fluctuations at y/c=0.01. The combined behavior of these fluctuations reflects the energy associated with the roll-up structures above the suction surface at x/c=0.05. For Ice-2, a similar trend is observed, with two peaks in the streamwise fluctuations as the distance from the surface increases. These fluctuations dissipate around y/c=0.03. For the crosswise fluctuations, one peak occurs at y/c=0.01, and the fluctuations diminish after y/c=0.02. Overall, the fluctuations in Ice-2 are more significant than those in Ice-1, which is in agreement with the observed distribution of turbulent kinetic energy in both cases.

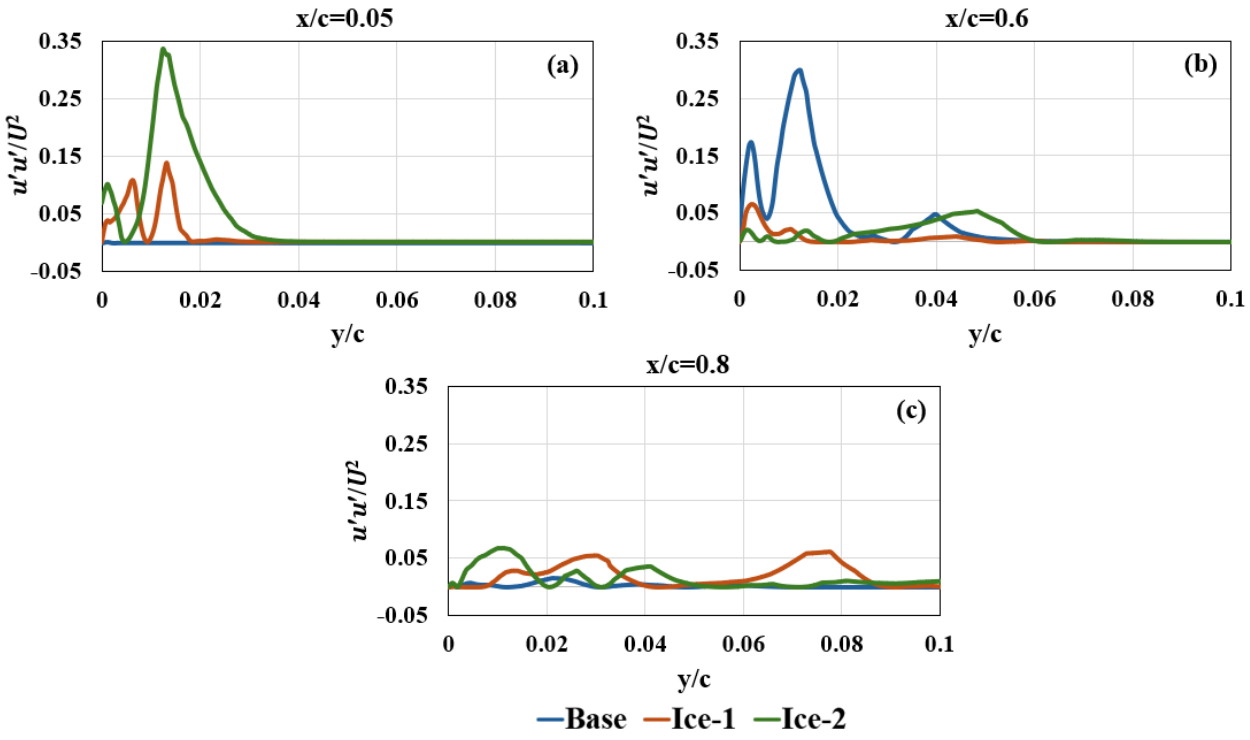

Figure 27: Streamwise Reynolds normal stress $u'u'$ distribution for Base, Ice-1 and Ice-2 at (a) x/c=0.05, (b) x/c=0.6 and (c) x/c=0.8.

Considering the fluctuations at x/c=0.6, where Base case experiences flow separation, as shown in Figure 27(b) and Figure 28(b), it can be observed that neither Ice-1 nor Ice-2 exhibit significant fluctuations in the streamwise or crosswise directions. This is due to the absence of separation and turbulent kinetic energy (TKE) distribution at this location, as previously discussed. In contrast, in Base, fluctuations are evident in both directions. In Figure 27(b), two peaks in streamwise fluctuations are observed at y/c=0.002 and y/c=0.012, whereas in the crosswise direction, a broader region of high fluctuation occurs between y/c=0.01 and y/c=0.03. Both fluctuations dissipate around y/c=0.05, which corresponds to the region with the highest TKE distribution in Base case at x/c=0.6.

At x/c=0.8, which is near the trailing edge of the airfoil, the flow in Base case remains largely attached to the surface, whereas in Ice-1 and Ice-2, flow separation has already occurred, as shown in Figure 20. As a result, fluctuations are expected in both the streamwise and crosswise directions, as depicted in Figure 27(c) and Figure 28(c). As anticipated, the magnitude of these fluctuations is lower compared to those at x/c=0.05, where Ice-1 and Ice-2 exhibit a higher turbulent kinetic energy distribution.

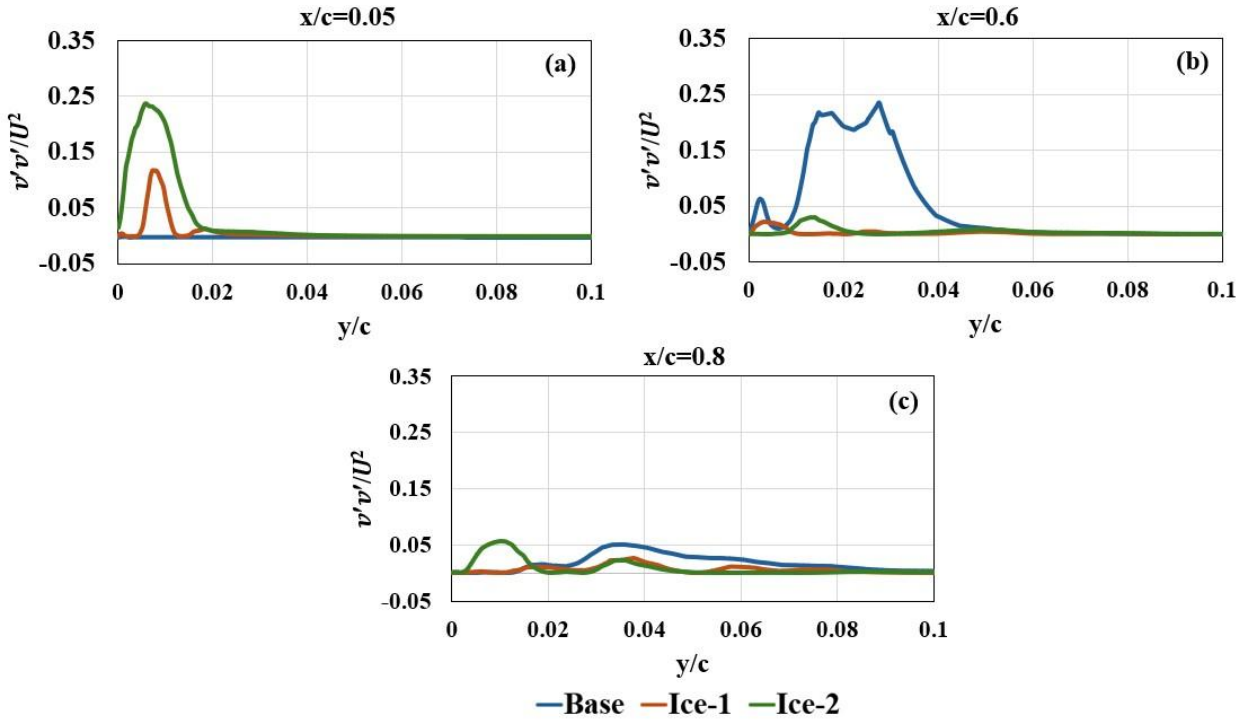

Figure 28: Crosswise Reynolds normal stress $v'v'$ distribution for Base, Ice-1 and Ice-2 at (a) x/c=0.05, (b) x/c=0.6 and (c) x/c=0.8.

A negative $u'v'$ indicates the transport of high-momentum fluid toward the wall or the movement of lower-momentum fluid away from it. Turbulent eddies facilitate this process by lifting low-momentum fluid from the near-wall region upward while sweeping high-momentum fluid from the outer flow downward. This exchange plays a crucial role in sustaining the turbulent boundary layer [33,69]. In regions of attached flow along the suction (upper) or pressure (lower) surfaces, a negative $u'v'$ enhances momentum transfer, which helps resist flow separation. This phenomenon promotes effective mixing, contributing to the maintenance of momentum near the surface, an essential factor for sustaining lift generation. Conversely, a positive $u'v'$ indicates the opposite effect, where fluctuations are correlated with the transport of low-momentum fluid toward regions of higher momentum, or vice versa. In flow separation regions, typically near the trailing edge or under strong adverse pressure gradients, the correlation between fluctuations can reverse. A positive $u'v'$ in these regions is associated with the development of recirculation zones or separation bubbles [27,28,70,71].

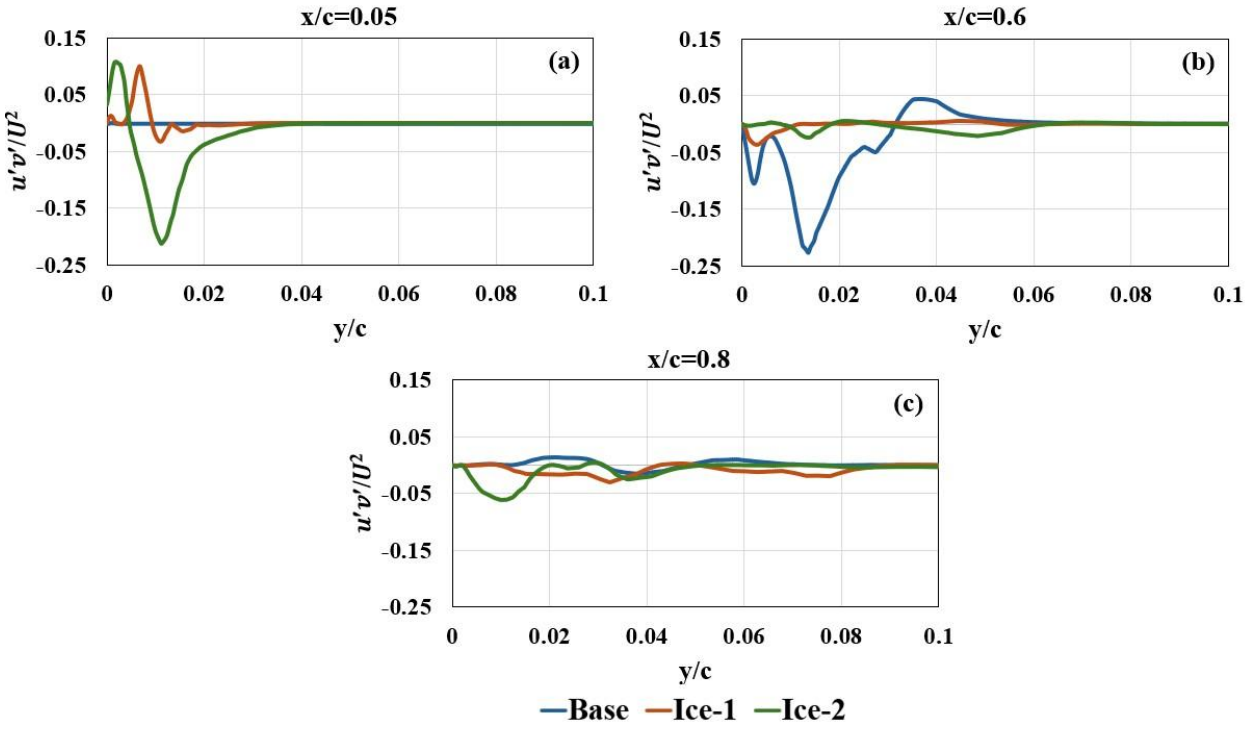

Figure 29: Reynolds shear stress $u'v'$ for Base, Ice-1 and Ice-2 at (a) x/c=0.05, (b) x/c=0.6 and (c) x/c=0.8.

Figure 29 presents the Reynolds shear stress based on streamwise and crosswise velocity fluctuations. As illustrated in Figure 29(a), at x/c=0.05, the fluctuation for Base case is negligible, whereas for Ice-1 and Ice-2, $u'v'$ is positive near the wall. This indicates that the fluctuations are correlated in a manner that facilitates the transport of low-momentum fluid toward regions of higher momentum, which aligns with the presence of the separation bubble on the leading edge. As the distance from the suction surface increases, the fluctuations in Ice-1 approach zero, while in Ice-2, they become negative. This negative value signifies the downward transport of high-momentum fluid from the outer flow toward the surface. A comparison with Figure 20(c) highlights that the end of the separation bubble corresponds to the region of positive $u'v'$, and as the flow moves farther from the surface, momentum mixing occurs, with high-momentum fluid being transferred to lower-momentum regions.

In Figure 29(b), it can be observed that there are no significant changes in $u'v'$ for Ice-1 and Ice-2 at x/c=0.6. This can be attributed to the fully attached flow, as shown in Figure 20(b) and Figure 20(c), where no distinct separation occurs. However, for Base case, a large negative region is present, indicating flow separation on the suction surface at x/c=0.6. The negative

values suggest that high-momentum flow from regions farther from the surface is being transported downward, replacing the lower-momentum fluid near the wall.

At x/c=0.8, since the flow has stabilized across all three cases, no significant variations in $u'v'$ fluctuations are observed for any cases, as shown in Figure 29(c).

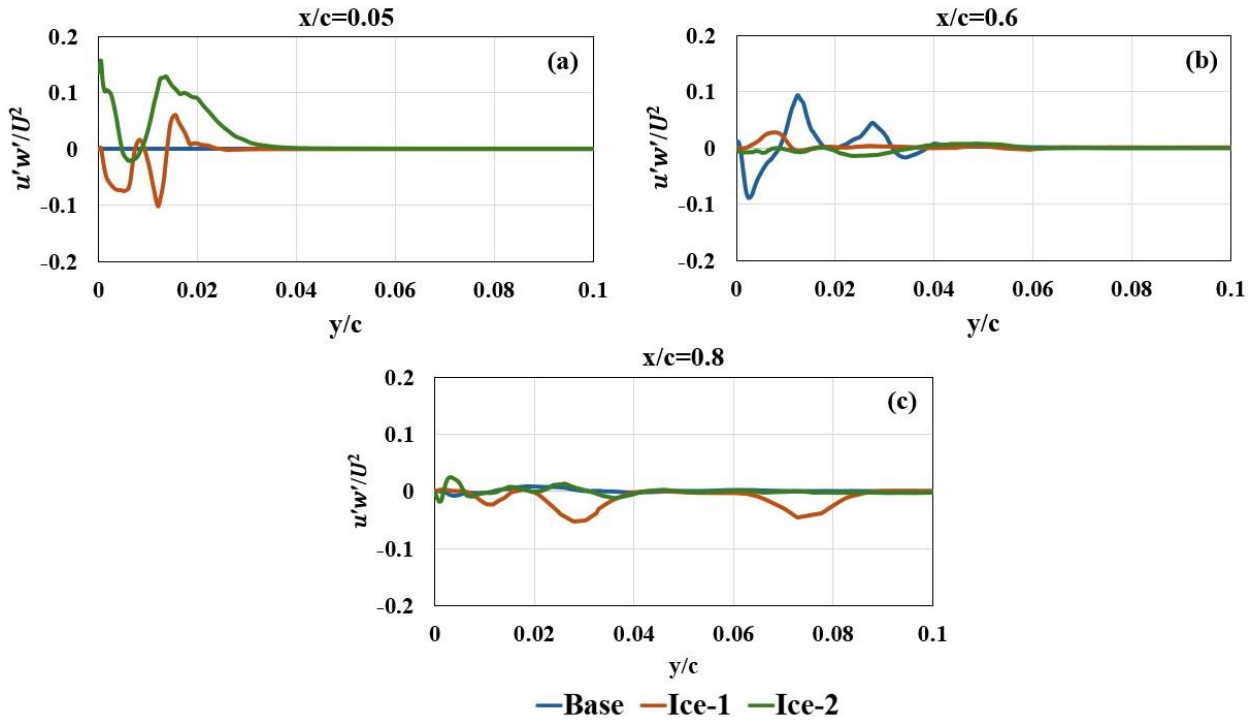

Figure 30: Reynolds shear stress $u'w'$ for Base, Ice-1 and Ice-2 at (a) x/c=0.05, (b) x/c=0.6 and (c) x/c=0.8.

A negative value of $u'w'$ indicates that when there is a positive fluctuation in the streamwise direction ($u' > 0$), it is typically accompanied by a negative fluctuation in the spanwise direction ($w' < 0$), and vice versa. This negative correlation suggests that turbulent eddies transport momentum in a manner that counteracts the spanwise mean gradient. In practical terms, it implies that high-speed fluid in the streamwise direction tends to move toward the center of the airfoil, while low-speed fluid is transported outward. In well-organized, attached flows over an airfoil, spanwise transport is generally moderated, and a negative $u'w'$ can reflect the influence of pressure gradients and surface curvature. These factors contribute to stabilizing the boundary layer, potentially delaying the three-dimensional instabilities that might lead to flow separation.

Conversely, a positive $u'w'$ indicates that a positive streamwise fluctuation ($u' > 0$) is correlated with a positive spanwise fluctuation ($w' < 0$), while negative fluctuations in the streamwise direction correspond to negative fluctuations in the spanwise direction. This correlation signifies that turbulent eddies are enhancing the spanwise transport of momentum, meaning high-speed fluid in the streamwise direction is being pushed outward along the airfoil, or vice versa. This behavior suggests that lateral mixing is being altered, often showing a transition in the flow structure due to separation or the emergence of complex vortical patterns.

As illustrated in Figure 31(a), while the fluctuation for Base case remains largely unchanged, both Ice-1 and Ice-2 exhibit positive and negative values, indicative of coherent structures being generated and dissipated. Around y/c=0.015, the maximum magnitude of $u'w'$ corresponds to the roll-ups observed in Figure 23 and Figure 24. In Figure 30(b), due to the attachment of the flow to the suction surface in Ice-1 and Ice-2, no significant variations in $u'w'$ are observed. However, in Base case, the presence of positive values suggests the initiation of roll-ups. Finally, Figure 30(c) shows no substantial variations across all three cases, as the predominant structures are oriented in the streamwise direction.

5. Conclusion

5.1. Conclusion

In the first part of the study the focus was on simulating the clean wind turbine airfoils with three cases of iced airfoils using LES (Large Eddy Simulation), in which two different ice profiles (Ice-1 and Ice-2) developed from experimental measurements [5] and one proposed parametric ice profile (Ice-3) [2] for five different angles of attack ranging from -10° to 10° with 5° step. The aerodynamic characteristics such as drag coefficient, lift coefficient, and aerodynamic performance of the two experimental ice profiles were examined and compared with Base case. For both Ice-1 and Ice-2 profiles, the lift coefficient increased consistently with an increase in the angle of attack, while the drag coefficient exhibited fluctuating behaviour. The aerodynamic performance for Ice-1 and Ice-2 increases to AoA=5° where it reaches its maximum while Base case achieved its highest efficiency in AoA=10°. In this angle of attack, both Ice-1 and Ice-2 displayed reduced efficiencies. In Ice-3, the drag coefficient trend closely followed that of Ice-1 between angles of attack of -5° and 10° and the lift coefficient showed an increase with the angle of attack. Similar to Ice-1 and Ice-2, Ice-3 experienced reduced efficiency at AoA=10° because of the stall, while it has its maximum performance at AoA=5°. It can be said that in all iced cases, the best performance is accelerated by 5° compared to Base case.

The second part of this study investigated the impact of ice accumulation on the aerodynamic performance of a wind turbine airfoil by analyzing the flow structures over an iced airfoil and comparing them with those of a clean airfoil. The focus was placed on examining coherent structures and turbulence kinetic energy (TKE) to understand how ice-induced surface modifications influence the flow behavior and aerodynamic efficiency. The findings show that ice accumulation significantly alters the flow field, leading to increased turbulence and disruption of coherent structures. The comparison between the clean and iced airfoils demonstrates that ice formation results in stronger and more irregular vortex structures, which contribute to higher levels of turbulence kinetic energy. These changes negatively affect the aerodynamic characteristics of the airfoil, increasing drag and reducing lift, ultimately impacting the efficiency of wind turbine blades in icy conditions. Furthermore, the study highlights the importance of accurately capturing flow instabilities and turbulence mechanisms in simulations of iced airfoils.

The observed variations in TKE and coherent structures emphasize the need for improved predictive models that account for ice accretion effects on aerodynamic performance.

5.2. Future work

Building on the findings of this study, several avenues for future research are proposed to enhance the understanding of ice accretion effects on wind turbine airfoil performance. A key focus will be to refine the characterization of ice shapes by incorporating region-specific data from a targeted area in Canada. This will involve detailed experimental measurements and field observations to capture the variation of ice accretion under local climatic conditions. These realistic ice profiles will then be integrated into computational simulations to better represent the actual conditions experienced by wind turbines in these regions.

In order to achieve a more accurate depiction of ice-induced modifications, the Discrete Phase Model (DPM) will be employed to simulate the ice formation process. The use of DPM is expected to provide a more comprehensive understanding of the deposition mechanisms and the evolution of ice shapes over time. This enhanced modeling approach will allow for the generation of ice profiles that are closely similar to those observed in the field, thereby improving the exactness of subsequent aerodynamic analyses.

Subsequently, simulations will be conducted to assess the aerodynamic performance of the airfoil under these more realistic icing conditions. The objective is to quantify the effects of the modified ice shapes on key aerodynamic parameters such as lift, drag, and turbulence kinetic energy (TKE). Insights from these simulations will be useful in identifying the critical areas where ice-induced flow disruptions are most noticeable, thereby guiding the optimization of de-icing and anti-icing strategies. The ultimate goal is to develop predictive models that can reliably forecast performance losses and assist in designing more effective de-icing systems for wind turbines.

Additionally, further research can be focused on a comparative analysis of different Large Eddy Simulation (LES) methodologies. By investigating the impact of various LES subgrid-scale models and their sensitivity to surface roughness effects, this work aims to refine the simulation framework used for predicting flow structures over iced airfoils. A more detailed exploration of

surface roughness, induced by ice accretion, will be conducted to better understand its influence on boundary layer dynamics and turbulence characteristics. This aspect of the study will provide valuable insights into how modifications in surface texture affect overall flow behavior and aerodynamic performance.

By addressing these research directions, future work will not only deepen the understanding of the complex interactions between ice accretion and aerodynamic performance but also contribute to the development of advanced simulation tools and optimization strategies. This integrated approach is anticipated to lead to significant improvements in the design and operation of wind turbines in cold climates, ultimately enhancing their efficiency and reliability under adverse icing conditions.

Bibliography

[1] H. Heng, F. Meng, J. McKechnie, Wind turbine blade wastes and the environmental impacts in Canada, Waste Manag. 133 (2021) 59–70. https://doi.org/10.1016/j.wasman.2021.07.032.

[2] S. Gantasala, N. Tabatabaei, M. Cervantes, J.O. Aidanpää, Numerical investigation of the aeroelastic behavior of a wind turbine with iced blades, Energies 12 (2019) 1–24. https://doi.org/10.3390/en12122422.

[3] S. Barber, Y. Wang, S. Jafari, N. Chokani, R.S. Abhari, The impact of ice formation on wind turbine performance and aerodynamics, J. Sol. Energy Eng. Trans. ASME 133 (2011) 1–9. https://doi.org/10.1115/1.4003187.

[4] O. Yirtici, I.H. Tuncer, S. Ozgen, Ice Accretion Prediction on Wind Turbines and Consequent Power Losses, J. Phys. Conf. Ser. 753 (2016). https://doi.org/10.1088/1742-6596/753/2/022022.

[5] B. Akay, D. Ragni, C.S. Ferreira, G.J.W. Van Bussel, Investigation of the root flow in a Horizontal Axis, Wind Energy (2013) 1–20. https://doi.org/10.1002/we.

[6] M.S. Virk, M.C. Homola, P.J. Nicklasson, Relation between angle of attack and atmospheric ice accretion on large wind turbine's blade, Wind Eng. 34 (2010) 607–613. https://doi.org/10.1260/0309-524X.34.6.607.

[7] S.G. Pouryoussefi, M. Mirzaei, M.M. Nazemi, M. Fouladi, A. Doostmahmoudi, Experimental study of ice accretion effects on aerodynamic performance of an NACA 23012 airfoil, Chinese J. Aeronaut. 29 (2016) 585–595. https://doi.org/10.1016/j.cja.2016.03.002.

[8] A.G. Kraj, E.L. Bibeau, Phases of icing on wind turbine blades characterized by ice accumulation, Renew. Energy 35 (2010) 966–972. https://doi.org/10.1016/j.renene.2009.09.013.

[9] A. Sundaresan, S. Arunvinthan, A.A. Pasha, S.N. Pillai, Effect of Ice accretion on the aerodynamic characteristics of wind turbine blades, Wind Struct. An Int. J. 32 (2021) 205–217. https://doi.org/10.12989/was.2021.32.3.205.

[10] L. Gao, Y. Liu, W. Zhou, H. Hu, An experimental study on the aerodynamic performance

degradation of a wind turbine blade model induced by ice accretion process, Renew. Energy 133 (2019) 663–675. https://doi.org/10.1016/j.renene.2018.10.032.

[11] L. Gao, Y. Liu, H. Hu, An experimental investigation of dynamic ice accretion process on a wind turbine airfoil model considering various icing conditions, Int. J. Heat Mass Transf. 133 (2019) 930–939. https://doi.org/10.1016/j.ijheatmasstransfer.2018.12.181.

[12] R.M. Imran, D.M.A. Hussain, M. Soltani, An experimental analysis of the effect of icing on Wind turbine rotor blades, Proc. IEEE Power Eng. Soc. Transm. Distrib. Conf. 2016-July (2016) 1–5. https://doi.org/10.1109/TDC.2016.7520041.

[13] Y. Han, J. Palacios, Analytical and experimental determination of airfoil performance degradation due to ice accretion, in: 4th AIAA Atmos. Sp. Environ. Conf. 2012, American Institute of Aeronautics and Astronautics Inc., 2012. https://doi.org/10.2514/6.2012-2794.

[14] M.C. Homola, M.S. Virk, T. Wallenius, P.J. Nicklasson, P.A. Sundsbø, Effect of atmospheric temperature and droplet size variation on ice accretion of wind turbine blades, J. Wind Eng. Ind. Aerodyn. 98 (2010) 724–729. https://doi.org/10.1016/j.jweia.2010.06.007.

[15] K. Szilder, W. Yuan, The influence of ice accretion on the aerodynamic performance of a UAS airfoil, 53rd AIAA Aerosp. Sci. Meet. (2015) 1–8. https://doi.org/10.2514/6.2015-0536.

[16] F. Villalpando, M. Reggio, A. Ilinca, Prediction of ice accretion and anti-icing heating power on wind turbine blades using standard commercial software, Energy 114 (2016) 1041–1052. https://doi.org/10.1016/j.energy.2016.08.047.

[17] M.C. Pedersen, H. Sørensen, Towards a CFD model for prediction of wind turbine power losses due to icing in cold climate, Open Arch. 16th Int. Symp. Transp. Phenom. Dyn. Rotating Mach. ISROMAC 2016 (2019).

[18] Q. Wang, X. Yi, Y. Liu, J. Ren, W. Li, Q. Wang, Q. Lai, Simulation and analysis of wind turbine ice accretion under yaw condition via an Improved Multi-Shot Icing Computational Model, Renew. Energy 162 (2020) 1854–1873. https://doi.org/10.1016/j.renene.2020.09.107.

[19] S. Li, R. Paoli, Modeling of ice accretion over aircraft wings using a compressible

openfoam solver, Int. J. Aerosp. Eng. 2019 (2019). https://doi.org/10.1155/2019/4864927.

[20] M. Sahin, T. Farsadi, Effects of Atmospheric Icing on Performance of Controlled Wind Turbine, IOP Conf. Ser. Earth Environ. Sci. 1121 (2022). https://doi.org/10.1088/1755-1315/1121/1/012011.

[21] D. Bodenlle-Toral, P. García-Regodeseves, A. Pandal-Blanco, Performance evaluation of an airfoil under ice accretion using CFD simulations, J. Phys. Conf. Ser. 2217 (2022). https://doi.org/10.1088/1742-6596/2217/1/012088.

[22] L.T. Contreras Montoya, A. Ilinca, S. Lain, Influence of Surface Roughness Modeling on the Aerodynamics of an Iced Wind Turbine S809 Airfoil, Processes 11 (2023). https://doi.org/10.3390/pr11123371.

[23] B. Bornhoft, S.S. Jain, K. Goc, S.T. Bose, P. Moin, Large-eddy simulations of the NACA23012 airfoil with laser-scanned ice shapes, Aerosp. Sci. Technol. 146 (2024) 108957. https://doi.org/10.1016/j.ast.2024.108957.

[24] I.K. Rotich, H. Chepkirui, Study on influence of turbulence intensity on blade airfoil icing mass & aerodynamic performance, Heliyon 10 (2024) e31859. https://doi.org/10.1016/j.heliyon.2024.e31859.

[25] H.L. Horning, Turbulence, 1921. https://doi.org/10.4271/210044.

[26] J.C.R. Hunt, a a Wray, P. Moin, Eddies, streams, and convergence zones in turbulent flows, Cent. Turbul. Res. Proc. Summer Progr. (1988) 193–208.

[27] D.C. Wilcox, Turbulence Modelling for CFD 3rd Edition, 1993. http://www.dcwindustries.com.

[28] W. Rodi, Comparison of LES and RANS calculations of the flow around bluff bodies, J. Wind Eng. Ind. Aerodyn. 69–71 (1997) 55–75. https://doi.org/10.1016/S0167-6105(97)00147-5.

[29] Y. Zhiyin, Large-eddy simulation: Past, present and the future, Chinese J. Aeronaut. 28 (2015) 11–24. https://doi.org/10.1016/j.cja.2014.12.007.

[30] H. Sarlak, Large Eddy Simulation of an SD7003 Airfoil: Effects of Reynolds number and Subgrid-scale modeling, J. Phys. Conf. Ser. 854 (2017). https://doi.org/10.1088/1742-

6596/854/1/012040.

[31] U. Shaukat, J.B. Jakobsen, N. Ikegaya, K.E.T. Giljarhus, Validation of Large Eddy Simulations in Urban Wind Studies Using a New Overall Area Metric, Available SSRN 4889659 267 (2024) 112285. https://doi.org/10.1016/j.buildenv.2024.112285.

[32] L. Davidson, Fluid mechanics, turbulent flow and turbulence modeling, Lecture Notes in MSc courses, Undefined (2023) 348.

[33] T. Jaroslawski, M. Forte, O. Vermeersch, J.M. Moschetta, E.R. Gowree, Disturbance growth in a laminar separation bubble subjected to free-stream turbulence, J. Fluid Mech. 956 (2023) 1–33. https://doi.org/10.1017/jfm.2023.23.

[34] T.A. Smith, Y. Ventikos, Boundary layer transition over a foil using direct numerical simulation and large eddy simulation, Phys. Fluids 31 (2019). https://doi.org/10.1063/1.5126663.

[35] S. Ghosal, P. Moin, The Basic Equations for the Large Eddy Simulation of Turbulent Flows in Complex Geometry, J. Comput. Phys. 118 (1995) 24–37. https://doi.org/10.1006/jcph.1995.1077.

[36] I.P. Castro, C. Vanderwel, Turbulent Flows: an Introduction, Turbul. Flows an Introd. (2021). https://doi.org/10.1088/978-0-7503-3619-2.

[37] W.W. Kim, S. Menon, A new dynamic one-equation subgrid-scale model for large eddy simulations, 33rd Aerosp. Sci. Meet. Exhib. (1995). https://doi.org/10.2514/6.1995-356.

[38] W.W. Kim, S. Menon, An unsteady incompressible Navier-Stokes solver for large eddy simulation of turbulent flows, Int. J. Numer. Methods Fluids 31 (1999) 983–1017. https://doi.org/10.1002/(SICI)1097-0363(19991130)31:6<983::AID-FLD908>3.0.CO;2-Q.

[39] J.V.N. de Sousa, A.G.B. de Lima, F.A. Batista, E.C. de Souza, D.C. de Macedo Cavalcante, P. de Morais Pessôa, J.E.F. do Carmo, On the Study of Autonomous Underwater Vehicles by Computational Fluid-Dynamics, 2020. https://doi.org/10.4236/ojfd.2020.101005.

[40] S. Mack, C. Brehm, B. Heine, A. Kurz, H.F. Fasel, Experimental investigation of separation and separation control on a laminar airfoil, 4th AIAA Flow Control Conf. (2008). https://doi.org/10.2514/6.2008-3766.

[41] B. Plogmann, S. Mack, H.F. Fasel, Experimental investigation of open- and closed-loop

control for airfoil under low Reynolds number conditions, 39th AIAA Fluid Dyn. Conf. (2009). https://doi.org/10.2514/6.2009-4282.

[42] I. Rodríguez, O. Lehmkuhl, R. Borrell, A. Oliva, Direct numerical simulation of a NACA0012 in full stall, Int. J. Heat Fluid Flow 43 (2013) 194–203. https://doi.org/10.1016/j.ijheatfluidflow.2013.05.002.

[43] I. Solís-Gallego, A. Meana-Fernández, J.M. Fernández Oro, K.M. Argüelles Díaz, S. Velarde-Suárez, LES-based numerical prediction of the trailing edge noise in a small wind turbine airfoil at different angles of attack, Renew. Energy 120 (2018) 241–254. https://doi.org/10.1016/j.renene.2017.12.082.

[44] R. Kojima, T. Nonomura, A. Oyama, K. Fujii, Large-eddy simulation of low-reynolds-number flow over thick and thin NACA airfoils, J. Aircr. 50 (2013) 187–196. https://doi.org/10.2514/1.C031849.

[45] M.C. Galbraith, M.R. Visbal, Implicit large eddy simulation of low-Reynolds-number transitional flow past the SD7003 airfoil, 40th AIAA Fluid Dyn. Conf. (2010). https://doi.org/10.2514/6.2010-4737.

[46] B.A. Lobo, A.P. Schaffarczyk, M. Breuer, Investigation into boundary layer transition using wall-resolved large-eddy simulations and modeled inflow turbulence, Wind Energy Sci. 7 (2022) 967–990. https://doi.org/10.5194/wes-7-967-2022.

[47] M.E. Rosti, M. Omidyeganeh, A. Pinelli, Direct numerical simulation of the flow around an aerofoil in ramp-up motion, Phys. Fluids 28 (2016). https://doi.org/10.1063/1.4941529.

[48] P. Ziadé, M.A. Feero, P. Lavoie, P.E. Sullivan, Shear Layer Development, Separation, and Stability over a Low-Reynolds Number Airfoil, J. Fluids Eng. Trans. ASME 140 (2018) 1–12. https://doi.org/10.1115/1.4039233.

[49] K. Asada, S. Kawai, Large-eddy simulation of airfoil flow near stall condition at Reynolds number 2.1 × 106, Phys. Fluids 30 (2018). https://doi.org/10.1063/1.5037278.

[50] D. Park, H. Shim, Y. Lee, PIV Measurement of Separation Bubble on an Airfoil at Low Reynolds Numbers, J. Aerosp. Eng. 33 (2020) 1–17. https://doi.org/10.1061/(asce)as.1943-5525.0001099.

[51] Chandrasekhar, Chandrasekhar1961, (1961).

[52] A. Winzen, B. Roidl, S. Klän, M. Klaas, W. Schröder, Particle-image velocimetry and force measurements of leading-edge serrations on owl-based wing models, J. Bionic Eng. 11 (2014) 423–438. https://doi.org/10.1016/S1672-6529(14)60055-X.

[53] W. Yuan, M. Khalid, J. Windte, U. Scholz, R. Radespiel, An investigation of Low-Reynolds-number flows past airfoils, Collect. Tech. Pap. - AIAA Appl. Aerodyn. Conf. 1 (2005) 102–120. https://doi.org/10.2514/6.2005-4607.

[54] J.R. Brinkerhoff, M.I. Yaras, Interaction of viscous and inviscid instability modes in separation-bubble transition, Phys. Fluids 23 (2011). https://doi.org/10.1063/1.3666844.

[55] Z. Yang, P.R. Voke, Large-eddy simulation of boundary-layer separation and transition at a change of surface curvature, J. Fluid Mech. 439 (2001) 305–333. https://doi.org/10.1017/S0022112001004633.

[56] P.R. Spalart, M.K. Strelets, Mechanisms of transition and heat transfer in a separation bubble, J. Fluid Mech. 403 (2000) 329–349. https://doi.org/10.1017/S0022112099007077.

[57] I.E. Abdalla, Z. Yang, Numerical study of the instability mechanism in transitional separating-reattaching flow, Int. J. Heat Fluid Flow 25 (2004) 593–605. https://doi.org/10.1016/j.ijheatfluidflow.2004.01.004.

[58] J. Zhou, R.J. Adrian, S. Balachandar, T.M. Kendall, Mechanisms for generating coherent packets of hairpin vortices in channel flow, J. Fluid Mech. 387 (1999) 353–396. https://doi.org/10.1017/S002211209900467X.

[59] Horváth, W. Bresky, J. Daniels, J. Vogelzang, A. Stoffelen, J.L. Carr, D.L. Wu, C. Seethala, T. Günther, S.A. Buehler, Evolution of an Atmospheric Kármán Vortex Street From High-Resolution Satellite Winds: Guadalupe Island Case Study, J. Geophys. Res. Atmos. 125 (2020) 1–28. https://doi.org/10.1029/2019JD032121.

[60] F.H. Clauser, The structure of turbulent shear flow, Nature 179 (1957) 60. https://doi.org/10.1038/179060a0.

[61] F. Course, A First Course in, New York (2003) 561.

[62] U. Frisch, Turbulence : The Legacy of A . N . Kolmogorov, (2018). https://doi.org/10.1017/CBO9781139170666.

[63] J.M. Cimbala, Experimental Study of Large Structure in the Far Wakes of Two-Dimensional Bluff Bodies., (1985).

[64] M. V Morkovin, Critical evaluation of transition from laminar to turbulent shear layers with emphasis on hypersonically travelling bodies, (1969).

[65] A. Roshko, Strearnwise vortex structure in plane mixing layers, J. Fluid Mech. 170 (1986) 499–525. https://doi.org/10.1017/S002211208600099X.

[66] W.S. Saric, H.L. Reed, E.B. White, Stability and transition of three-dimensional boundary layers, Annu. Rev. Fluid Mech. 35 (2003) 413–440. https://doi.org/10.1146/annurev.fluid.35.101101.161045.

[67] I. Solís-Gallego, K.M.A. Díaz, J.M.F. Oro, S. Velarde-Suárez, Wall-resolved LES modeling of aWind turbine airfoil at different angles of attack, J. Mar. Sci. Eng. 8 (2020). https://doi.org/10.3390/jmse8030212.

[68] P. Ekman, J. Venning, T. Virdung, M. Karlsson, Importance of sub-grid scale modeling for accurate aerodynamic simulations, J. Fluids Eng. Trans. ASME 143 (2021). https://doi.org/10.1115/1.4048351.

[69] J.E. Park, Pr ep rin t n ot pe er r ed Pr ep rin t n ot pe er ed, (2017).

[70] P. Morra, O. Semeraro, D.S. Henningson, C. Cossu, On the relevance of Reynolds stresses in resolvent analyses of turbulent wall-bounded flows, J. Fluid Mech. 867 (2019) 969–984. https://doi.org/10.1017/jfm.2019.196.

[71] M. Baungaard, S. Wallin, M.P. Van Der Laan, M. Kelly, Wind turbine wake simulation with explicit algebraic Reynolds stress modeling, Wind Energy Sci. 7 (2022) 1975–2002. https://doi.org/10.5194/wes-7-1975-2022.